NANO · MICRO small
www.small-journal.com

Phosphorus-Based Materials for High-Performance Alkaline Metal Ion Batteries: Progress and Prospect

*Linchao Zeng, Licong Huang, Jianhui Zhu, Peipei Li, Paul K. Chu, Jiahong Wang, and Xue-Feng Yu**

Alkaline metal-ion batteries (AIBs) such as lithium-ion batteries (LIBs), sodium-ion batteries (NIBs), and potassium-ion batteries (KIBs) are potential energy storage systems. Currently, although LIBs are widely used in consumer electronics and electric vehicles, the electrochemical performance, safety, and cost of current AIBs are still unable to meet the needs for many future applications, such as large-scale energy storage, due to the low theoretical capacity of cathode/anode materials, flammability of electrolytes and limited Li resources. It is thus imperative to develop new materials to improve the properties of AIBs. Several promising cathodes, anodes, and electrolytes have been developed and among the new battery materials, phosphorus-based (P-based) materials have shown great promise. For example, P and metal phosphide anodes have high theoretical capacity, resource abundance, and environmental friendliness boding well for future high-energy-density AIBs. Besides, phosphate cathode materials have the advantages of low cost, high safety, high voltage, and robust stability, and P-based materials like $LiPF_6$ and lithium phosphorus oxynitride are widely used electrolytes. In this paper, the latest development of P-based materials in AIBs, challenges, effective solutions, and new directions are discussed.

1. Introduction

Renewable energy is a promising way to rid our dependence on fossil, but renewable energy sources like wind energy and solar energy rely heavily on natural conditions such as the terrain and climate and can be geographically and intermittently difficult to connect directly to the electrical grid.[1] To utilize these energy sources efficiently and timely, advanced energy storage devices (ESDs) must be able to store and export the energy efficiently.[2,3] In addition, in order to meet the portability and mobility of electronic products such as cell phones and computers, it is particularly important to develop advanced ESDs. Rechargeable alkaline-ion batteries (AIBs), including lithium-ion batteries (LIBs), sodium-ion batteries (NIBs), and potassium-ion batteries (KIBs) are revolutionary and LIBs are widely used in portable consumer electronics and electric vehicles. However, Li is not abundant on earth and difficulties in Li ore mining have raised the price thereby hampering wider application of LIBs to large-scale energy storage.[4] In recent years, NIBs and KIBs have attracted considerable attention as an alternative energy storage systems to LIBs. This is due to the following several reasons. First, Na and K, which are in the same chemical group as Li, have similar chemical properties as Li and development of NIBs and KIBs can be based on knowledge gained on LIBs.[5,6] Besides, the Na reserve in the earth crust is three orders of magnitude bigger than that of Li making NIBs more economical. So far, NIBs have made some progress in industrial development in stationary energy storage and low-speed transportation. Although K is inferior to Na in terms of reserve and cost, the redox potential of K is higher than of Na and graphite materials commonly used in LIBs can serve as the negative electrode materials in KIBs (specific capacity is about 250 mAh g^{-1}).[7]

The materials used in the anode, cathode, and electrolyte determine the properties of batteries such as the cyclic stability, rate, and safety. At present, the capacities of anode and cathode materials in AIBs are limited and phosphorus-based (P-based) materials have garnered interest as cathodes, anodes, electrolytes, and separators of batteries due to advantages such as environmental protection, safety, low cost, availability, and good electrochemical characteristics. In particular, red P and black P are promising candidates due to their abundant reserve and high theoretical specific capacity (2596 mAh g^{-1} for AIBs).[8,9] Although red P is commercially available and easy to handle, it has low electrical conductivity ($\approx 10^{-14}$ S m^{-1}) and shows poor reversibility in electrochemical reactions.[9] Crystalline black P

L. Zeng, L. Huang, J. Zhu, J. Wang, X.-F. Yu
Materials Interfaces Center
Shenzhen Institute of Advanced Technology
Chinese Academy of Sciences
Shenzhen 518055, P. R. China
E-mail: xf.yu@siat.ac.cn

P. Li
School of Materials Science and Engineering
Hefei University of Technology
Hefei 230009, P. R. China

P. K. Chu
Department of Physics
Department of Materials Science and Engineering
and Department of Biomedical Engineering
City University of Hong Kong
Tat Chee Avenue, Kowloon, Hong Kong 999077, P. R. China

The ORCID identification number(s) for the author(s) of this article can be found under https://doi.org/10.1002/smll.202201808.

DOI: 10.1002/smll.202201808

 © 2022 Wiley-VCH GmbH

as anode materials has better electrochemical reversibility than red P because of the layered structure of corrugated sheets and relatively high electrical conductivity (≈300 S m^{-1}).[10] Metal phosphides have also been widely studied as anode materials for AIBs on account of the high specific capacity, suitable redox potential, metallic properties, and excellent thermal stability. As cathode materials determine the performance of AIBs, research on cathode materials is a hot spot. Among the various materials, polyanionic materials are considered one of the attractive options for AIBs. Owing to the inductive effects of polyanionic groups, polyanionic materials have larger working potentials and the robust 3D framework mitigates structural changes during extraction and insertion of Li^+/Na^+, while preserving the stability of the extraction and insertion potentials of Li^+/Na^+. For example, lithium iron phosphate polyanionic materials have been industrialized and widely used as cathode materials in LIBs due to the high electrochemical potential, good cyclic stability, low cost, and actual specific capacity close to the theoretical limit (≈165 mAh g^{-1}).[11,12] Lithium phosphorous oxynitride (LiPON) films are widely used as electrolyte films in all-solid-state thin-film LIBs because of the high Li^+ conductivity (2.0×10^{-6} S cm^{-1}), low activation energy (0.45 eV), and electrochemical stability window as wide as 5.5 V.[13,14]

In order to develop high-performance AIBs with P-based materials, it is necessary to understand the challenges of P-based materials including the inherently low electrical conductivity of phosphate polyanionic cathodes and large volume expansion of P-based anodes. Some effective strategies to improve the electrodes are materials compounding, adoption of nanocrystalline materials, and controlling the morphology of materials.[15,16] Materials compounding combines the characteristics of different materials, often time synergistically, to minimize the shortcomings of single materials and obtain functions and properties that single materials cannot provide. For example, the low electrical conductivity of the red P anode and phosphate polyanionic cathode can be overcome by compounding with conductive materials. Studies have shown that nanoscale materials can alleviate the volume expansion and pulverization of P-based anode materials during charging/discharging.[17–20] In addition, nanocrystalline electrode materials increase the contact with the electrolyte, shorten the diffusion path of ions, facilitate rapid transfer of external ions to the electrode materials, and improve the reaction kinetics of batteries. It is well known that nanostructured materials have a large surface area, which leads to the formation of more solid electrolyte interphase (SEI) during the initial charging and discharging processes and a lower initial coulomb efficiency (ICE) of electrode materials, adversely affecting battery performance. Therefore, it is very important to design the morphology of electrode materials to control the formation of SEI during battery cycling. For example, interconnected porous conductive networks with multidimensional hierarchical building blocks and controllable pore structure can balance diffusion and transfer of electrons and ions to stabilize the formation of SEIs.

This paper reviews the potential applications of P-based materials to the anode, cathode, and electrolyte in AIBs (**Figure 1**). With regard to the anode, the influence of advanced structural design including 1D, 2D, and 3D structures on the electrochemical properties of P-based anode materials is discussed. As for the cathode, the relationship between the composition, structure, and electrochemical properties of phosphate polyanionic materials is reviewed from the perspectives of the crystal structure, storage mechanism, and modification strategy. Finally, the application of P-based materials to electrolytes such as electrolyte salts, solid electrolytes, and fire-retardant additives in AIBs is discussed.

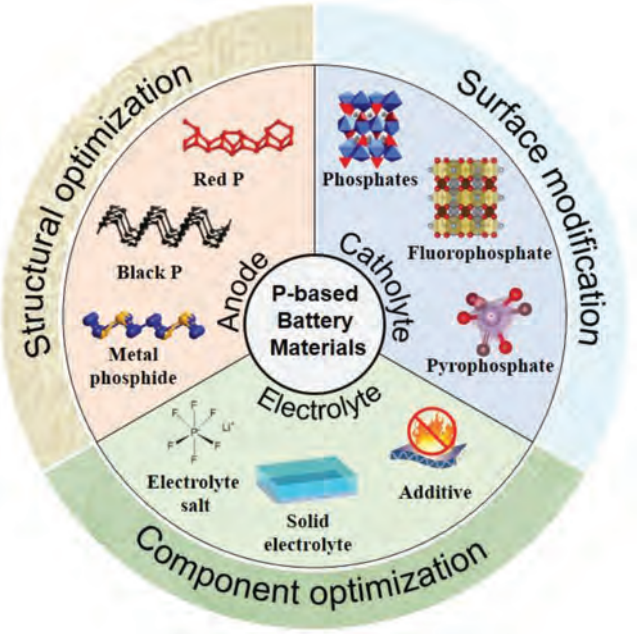

Figure 1. The potential application of P-based materials in alkaline metal ion batteries (AIBs) and corresponding material design and modification methods.

2. P-Based Anode Materials

P is a nonmetallic element with three main allotropes, namely white P, red P, and black P. White P has a highly symmetrical P_4 tetrahedral structure with weak intermolecular interactions, resulting in chemically unstable, volatile, toxic, and flammable properties, which are not suitable for electrode materials.[21] Red P has a polymer structure with chains or rings formed by P_4 tetrahedron single bonds with high stability.[8] Red P is promising as anode materials in AIBs on account of the high specific capacity (2596 mAh g^{-1}) and easy treatment. However, its electrical conductivity is low (≈10^{-14} S m^{-1}) and it should be combined with a conductive matrix to form the anode in AIBs. Black P has high electrical conductivity and a folded lamellar structure and is similar to graphite in the appearance, properties and structure. The interlayer distance of black P (5.3 Å) is larger than that of graphene (3.3 Å), rendering it easier for ions to be inserted to boost the ion conductivity.[22] First-principles calculation shows that the folded structure of black P can provide ultrafast diffusion channels for Li^+/Na^+, suggesting the potential of black P as host materials for Li^+/Na^+ intercalation.[23,24] Owing to the structural advantages, excellent thermodynamic stability, and high theoretical specific capacity (2596 mAh g^{-1}), black P has been studied as anode materials

© 2022 Wiley-VCH GmbH

in AIBs. Black P can be exfoliated into monolayers or layered 2D nanosheets and black P films with atomic thickness are known as "phosphorene."[25] The 2D structure endows phosphorene with unique energy storage advantages such as shorter ion diffusion paths and higher active site utilization.[26] Metal phosphides have also been widely studied as anode materials in secondary batteries due to the good electrical conductivity and electrochemical characteristics.[27] Energy storage and output between metal phosphide and alkali metal ions proceed by transformation and alloy reactions, thus providing a higher specific capacity than the P anode. However, both the P anode and metal phosphide anode are prone to volume expansion and low electrical conductivity in AIBs and so the materials must be modified. In this section, according to the structural characteristics of modified red P, black P and metal phosphating composite anodes, the materials are divided into 1D, 2D, and 3D nanostructures. Advanced structural design of electrodes and the impact on the electrochemical performance of alkali metal ion storage are discussed to reveal the effective strategy for the design and preparation of high-performance P-based anode materials.

2.1. Red P

As promising anode materials in AIBs, red P has the advantages of natural abundance, low cost, environmental friendliness good chemical stability, and high theoretical specific capacity. Owing to the poor electrical conductivity of red P, early studies show that the charging/discharging capacity of red P is too small to be useful as anode materials in batteries. However, adding carbonaceous materials to red P anodes can increase the charging and discharging capacity as well as reversibility of batteries mainly due to the enhanced electrical conductivity and mechanical stability of the electrode. Liu et al. have used ball milling to uniformly wrap fluffy carbon around red P particles and the red P/carbon composite shows a reversible capacity of 1230 mAh g^{-1} during cycling at a current density of 2.6 A g^{-1} as a result of the improved electrical conductivity of the electrode materials. In addition to the poor electrical conductivity, red P undergoes huge volume expansion during charging/discharging giving rise to collapse of electrode structure and degraded battery properties.[28] Some studies have shown that amorphous red P has a better capability to accommodate the volume expansion during Li^+/Na^+ insertion and extraction than crystalline red P. The amorphous structure of red P makes expansion isotropic consequently reducing the volume expansion rate of the electrode and protecting the electrode from serious damage.[29,30] Therefore, the Li^+/Na^+ storage capacity of red P largely depends on the morphology and crystal structure and advanced structural design can improve the electrochemical characteristics of red P anodes.[20,31,32]

2.1.1. 1D structures

Carbon nanotubes (CNTs) are 1D carbon materials with special structural characteristics. CNTs have radial dimensions of only nanometers and axial lengths of tens to hundreds of micrometers.[33] According to the number of graphite sheets on the tube wall, CNTs can be divided into single-walled carbon nanotubes (SWCNTs) and multiwalled carbon nanotubes (MWCNTs). Carbon atoms on the CNT (CNT: carbon nanotube) are sp^2 hybridized and bond with each other to form a honeycomb structure of the hexagon CNT skeleton. The unhybridized pair of p electrons on each carbon atom forms a conjugated Π electron cloud over the entire CNT and CNTs have unique physicochemical properties such as superconductivity and high mechanical strength.[34–36] Unlike carbon particles, which act as loose substrates and confine red P through pores, CNTs with high aspect ratios and mechanical strength act more like ropes that binding red P together. For example, CNTs form a network of connections between red P and the charging/discharging capacity, high-current density charging-discharging capability, and cyclic stability of red P electrodes can be improved by embedding amorphous red P into the CNTs network. It is worth noting that the improvement in the electrochemical properties of the electrode materials is limited after combining red P and CNTs or by ball milling because red P cannot fill the voids between the CNTs well.[37–39]

In order to create better physical interactions, Zhu et al. have diffused P vapor into the interspaces between entangled SWCNTs bundles by an improved evaporation-condensation method and good dispersion of red P between SWCNTs bundles is achieved.[40] Using this nondestructive method, the red P-SWCNTs composite retains the high electrical conductivity and mechanical strength of the SWCNTs network. As a result, the red P-SWCNTs composite electrode exhibits good rate capability of ≈300 mAh g^{-1} at 2 A g^{-1} and good cyclic stability with capacity retention rate of 80% after 2000 cycles at 2 A g^{-1} for storage of Na^+ (**Figure 2**a). The excellent electrochemical performance proves that CNTs can improve electron conduction and inhibit the volume expansion of red P to prevent pulverization. Yun et al. have fabricated vertically aligned CNT with an average diameter of 75 nm using porous alumina templates and encapsulated red P into the CNT to prepare red P nanowire arrays (P@CNWs) (Figure 2b).[41] The P@CNWs anode has a high specific capacity of 2250 mAh g^{-1} and ICE of 83% in NIBs. The improved electrochemical properties of the P@CNWs electrode arise from the vertically aligned CNT structure that provides a porous and highly conductive network for transportation of ions and electrons. The uniform channels of CNWs also accommodate the volume expansion of red P during electrochemical cycling, which is beneficial to the formation of stable SEI films.

Incorporation of red P into porous carbon nanofibers (PCNFs) by evaporation-condensation-conversion (VCC) is a promising strategy to prepare high-performance red P-carbon electrodes. The PCNFs matrix not only establishes an interconnected conductive network among independent P particles but also buffers the volume change of P during charging/discharging due to the porous structure. Li et al. have designed a self-supported flexible electrode by loading red P crystal into PCNFs by a VCC strategy (Figure 2c) and used it in the anode material of LIBs.[32] The composite anode (P-PCNFs) shows excellent cycling characteristics (2030 mAh g^{-1} at 0.26 A g^{-1} after 100 cycles) and rate capability (380 mAh g^{-1} at 2.9 A g^{-1}). At present, electrospinning is one of the main methods to prepare PCNFs due to the simple manufacturing device, low

 © 2022 Wiley-VCH GmbH

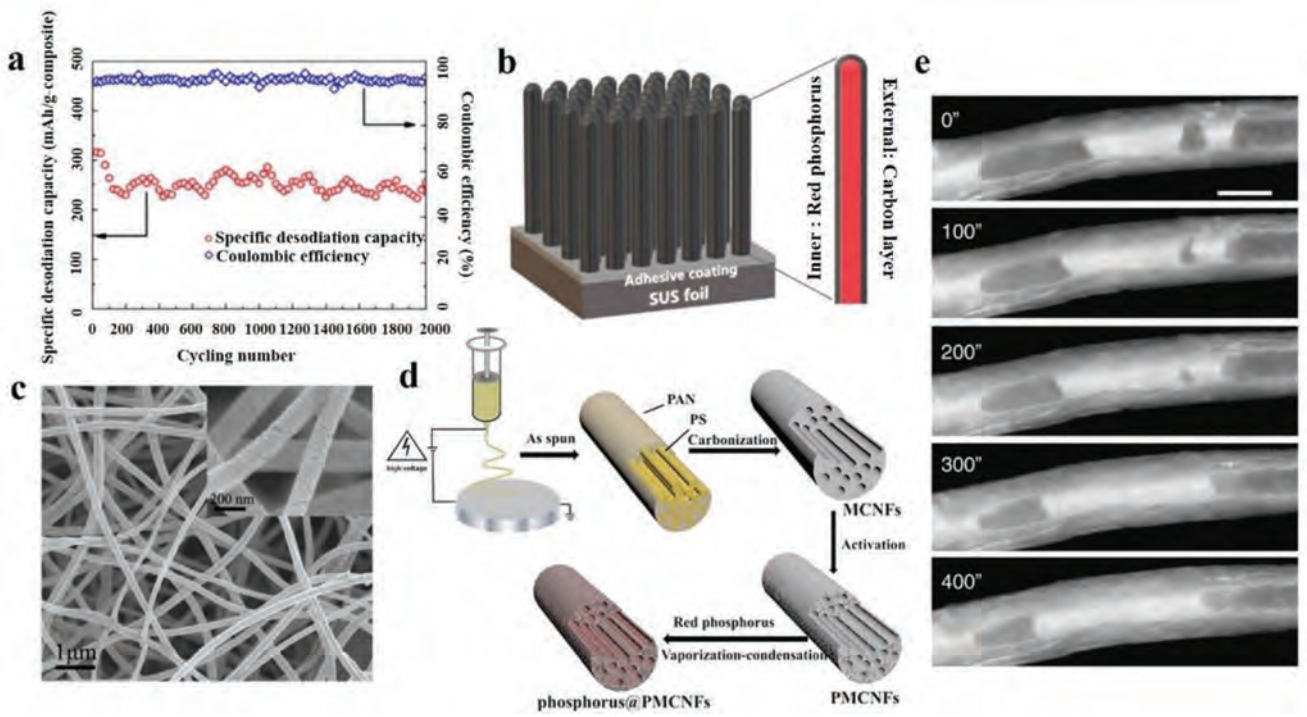

Figure 2. a) Cycling characteristics of P@CNWs. Reproduced with permission.[40] Copyright 2015, American Chemical Society. b) Schematic illustration of the P@CNWs electrode after removal of the Al foil and alumina by a wet etching step. Reproduced with permission.[41] Copyright 2021, MDPI. c) FE-SEM micrograph of P-PCNFs.[32] Copyright 2014, Elsevier. d) Schematic illustration of the fabrication process of P@PMCNFs. Reproduced with permission.[42] Copyright 2017, Elsevier. e) STEM image series captured in real-time showing two red P segments merging during sodiation. Reproduced with permission.[43] Copyright 2020, Springer Nature.

spinning cost, controllable process, and wide variety of spinnable materials. Sun et al. have encapsulated red P in 1D porous multichannel hollow carbon nanofibers (P@PMCNFs) by electrospinning and vaporization-condensation (Figure 2d).[42] As a self-supported electrode in NIBs, the materials exhibit excellent rate capability (500 mAh g^{-1} at 10 A g^{-1}) and long cycling life (700 mAh g^{-1} at 2 A g^{-1} after 920 cycles). In this composite, the nanoscale P is accommodated in a highly conductive self-supported interconnected nanofiber mesoporous structure that provides rapid diffusion channels for Na^+ and electrons, thereby achieving superior rate capability. In addition, the porous structure of PCNFs alleviates the mechanical damage caused by the volume expansion of red P consequently improving the cycling characteristics and structural stability of the electrode. This self-supporting, nonbinder electrode design simplifies the manufacturing process and is a promising solution to improve the electrochemical properties of AIBs.

The electrode consisting of the composite of red P and 1D PCNFs has good cyclic stability but it is not related to only the constraint of carbon fibers, but also the special properties of red P. Liu et al. have investigated the sodiation process of the synthesized red P-impregnated carbon nanofibers (CNFs) composite (red P@CNFs) by in situ transmission electron microscopy and chemical mechanical simulation.[43] The results show that the softening of red P particles during sodiation undergoes large volume expansion through longitudinal expansion along the inner space of the CNFs without causing significant deformation or cracking of the hard CNFs shell (Figure 2e). As a result, the red P@CNFs anode has a high reversible capacity of 1850 mAh g^{-1} for 500 cycles at 0.1 A g^{-1} as well as a reversible capacity exceeding 1000 mAh g^{-1} for 5000 cycles.[43] The study also discloses that the observed "liquefaction" phenomenon arises from the intrinsic properties of red P but not electron beam-induced heating effects, which are not observed from other allotropes such as black P.[44–46] The "liquid-like" mechanical behavior of red P to some extent reveals the reason for the enhanced cyclic stability of red P wrapped by porous carbon nanofibers and it is of great significance in the design of high-performance red P-based anodes.

2.1.2. 2D structures

The way and properties of electrode materials to store Li^+ depend on the structure and morphology. 2D nanostructures have a large surface area and can provide usable free space in the planar direction to buffer the large volume expansion and release mechanical strain to boost the long-term cyclic stability. Owing to the large exposed active surface and nanoscale thickness, the solid-state transportation paths of ions are shortened thus enabling fast insertion and storage of alkali metal ions.

Graphene is one of the most attractive classes of 2D carbon materials boasting high electrical conductivity, large surface area, and high flexibility. When graphene is used as the matrix for red P, these excellent properties enable close interfacial contact between graphene and red P, so that the dispersed P

 © 2022 Wiley-VCH GmbH

particles are anchored properly to mitigate aggregation of P particles during volume change. Song et al. have developed a chemically bonded P/graphene mixture by simple ball milling of red P and graphene stacks.[47] During ball milling, strong P—C and P—O—C chemical bonds are formed to promote the contact between P and graphene nanosheets and improve the overall conductivity of the electrode and stability of the SEI layer (**Figure 3**a). As a result, the P/graphene nanosheet anode exhibits high ICE of 83% and excellent cyclic stability of 1700 mAh g^{-1} after 60 cycles for storage of Na^+. Liu et al. have prepared the nanoporous red P@graphene oxide composite (NPRP@RGO) by redox reaction and boiling.[48] Owing to the unique porous structure of nano red P and highly electronically conductive network constructed on the RGO sheet, migration of ions and electrons is facilitated and the volume expansion is buffered (Figure 3b). The NPRP@RGO electrode has excellent rate properties of 971.7 mAh g^{-1} at 5.12 A g^{-1} and long cycling life of 775.3 mAh g^{-1} at 5.12 A g^{-1} after 1500 cycles for storage of Na^+. This simple boiling method expands the synthetic routes of nanoporous structures composed of red P anodes for high-performance AIBs.

Under mild conditions, red P and graphene composites with good properties can be obtained by simple suction filtration. As shown in Figure 3c, Wang et al. have prepared red P nanoparticles with a uniform size distribution by ultrasonic/centrifugal method and graphene nanoribbons (GNR) are prepared by cofiltration to synthesize the composite of red P and graphene nanoribbons (RP-GNR) for anodes in LIBs.[49] Electrochemical tests show that the capacity retention of RP-GNR (RP, 39 wt%) is 87% after 545 cycles at 1 A g^{-1} and GNR and red P can form close contact to improve the electrical conductivity by co-filtration. In the RP-GNR composite, increasing the GNR content enhances the rate performance. This study suggests a safe, convenient, economical, and scalable solution to prepare high-performance red P anodes.

2D layered MXenes have attracted great interest in the field of ESDs due to their unique physical and chemical properties, such as the metallic conductivity, tunable interlayer spacing, and excellent mechanical properties. Electrodes based on MXenes or materials combining MXenes with different active materials are widely used in AIBs. Zhang et al. have prepared a N-doped $Ti_3C_2T_x$ and P composite (N-$Ti_3C_2T_x$/P) by spray drying and vapor deposition.[50] The red P particles penetrate the interlayer of the N-$Ti_3C_2T_x$ matrix to form stable Ti—O—P bonds to prevent aggregation and loss of red P and promote transportation of ions and electrons. The interlayer spacing of the N-$Ti_3C_2T_x$ matrix is variable to avoid the electrode from pulverization caused by the volume expansion of P during electrochemical cycling. As a result, the N-$Ti_3C_2T_x$/P exhibits excellent cyclic stability up to 1040 cycles without capacity fading in storage of Li^+. The MXenes and red P composites prepared by vapor deposition are simple and versatile and have

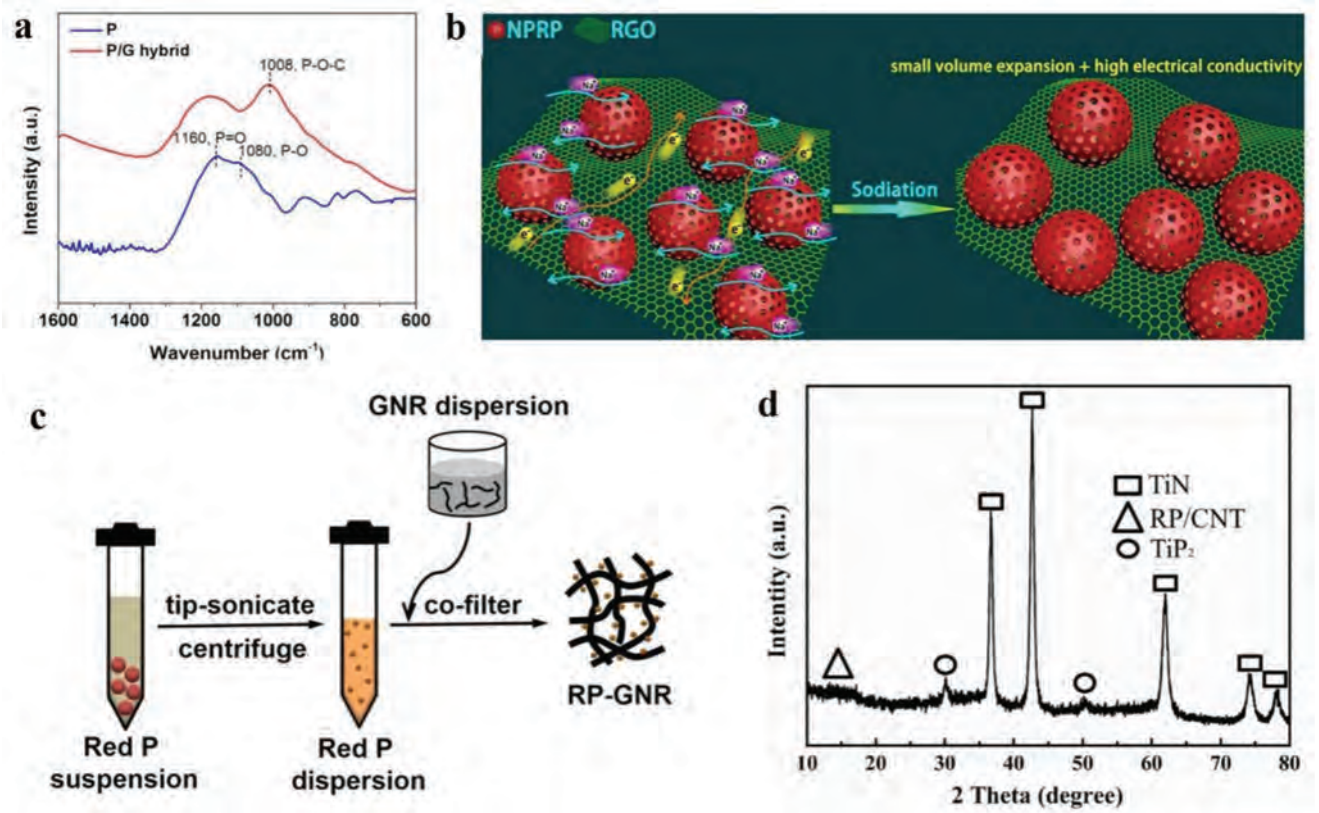

Figure 3. a) FTIR spectra of the ball-milled P and P/G hybrid. Reproduced with permission.[47] Copyright 2014, American Chemical Society. b) Schematic showing sodiation the NPRP@RGO anode in NIBs. Reproduced with permission.[48] Copyright 2018, American Chemical Society. c) Schematic illustration of the preparation of the RP-GNR composite by tip-sonication and cofiltration. Reproduced with permission.[49] Copyright 2018, American Chemical Society. d) XRD pattern of the red P/TiN/CNT composite. Reproduced with permission.[51] Copyright 2020, Elsevier.

 © 2022 Wiley-VCH GmbH

broad application prospects. The electrochemical properties of MXenes/Red P composites can be optimized with different MXenes matrices and surface modification.

As advanced 2D structural materials, TiN nanosheets not only have excellent electrochemical corrosion resistance and good electrical and Li^+ conductivity, but also can form strong and stable chemical bonds with P at the interface. Han et al. have embedded amorphous soft red P nanoparticles into TiN nanosheets and CNTs by high-energy ball milling to form a conductive TiP_2 layer at the interface between red P and TiN in situ (Figure 3d).[51] The TiP_2 layer enhances diffusion of Li^+ and inhibits the side reactions between P and electrolyte to improve the reaction kinetics and interface stability of red P. The red P/TiN/CNT delivers excellent rate performance such as a high reversible capacity of 868.7 mAh g^{-1} at a large current density of 2.3 A g^{-1} as well as long-term cycling with the capacity retention rate from the 3rd to 850th cycle of 96.9%. The idea of designing modified interfacial materials to accelerate the electrochemical kinetics and inhibit the formation of resistive SEI is of great significance in rapid charging of P-based anodes and improving the ICE.

2.1.3. 3D Structures

As the volume of P changes greatly in the phase transformation to Li_3P, leading to severe pulverization of red P, formation of a large number of pulverized P particles electrically isolated in the anode, and rapid degradation of the electrochemical performance. Reducing the size of red P can alleviate the severe strain caused by the huge volume change during electrochemical cycling and improve the cyclic stability. High-energy mechanical milling is a simple and efficient method to decrease the particle size and is widely used in the preparation of nanoscale red P particles. In order to improve the overall conductivity of the electrode, red P and conductive carbon materials are usually ball-milled together to form a 3D stacked structure with uniform distributions of red P and carbon. Qian et al. have used high-energy mechanical milling to compound amorphous red P with carbon black (or super P) at room temperature.[52] P—O—C chemical bonds are formed in the hybrids to improve the electrical conductivity, enhance the P/carbon black contact, and increase the structural durability. The anode materials have good cycling characteristics such as 90% capacity retention after 100 cycles at 2 A g^{-1} and 62% capacity retention at a high current of 8 A g^{-1}. The red P/carbon black composite has been prepared by a similar method and the Na^+ storage properties have been investigated.[53] The composite has a specific capacity exceeding 800 mAh g^{-1} after 140 cycles because homogeneous dispersion of red P in the carbon matrix buffers the volume change of red P during charging/discharging.

Encapsulating red P in the voids of the 3D porous carbon matrix can reduce the adverse effects of volume expansion of red P during electrochemical cycling. Marino et al. have prepared an activated carbon/P composite by vaporization-condensation-conversion.[31] The porous parts of the activated carbon are filled with P and the contact between P and activated carbon is close. Transfer of electrons from P to carbon completes the "electrochemical activation" of P and Li^+. Wang et al. have prepared a red P/activated carbon composite with a high P concentration (60.0 wt%) and reversible capacity up to 1550 mAh g^{-1}.[54] Using P_4O_{10} and polyethylene glycol as raw materials, Sun et al. have prepared a carbon/P composite with a 3D structure by carbon reduction (**Figure 4**a).[55] By means of the bottom-up approach, a composite composed of ultrafine red P particles (≈10 nm) that are tightly connected to the 3D carbon framework via P—O—C bonds is obtained. In the composite, the P—O—C bond ensures good electrical contact between P and the carbon matrix and the ultrafine red P nanoparticles can adapt to the expansion stress and reduce the diffusion length without breaking. The 3D carbon/P composite shows a high reversible capacity of 920 mAh g^{-1} at 0.21 A g^{-1} after 160 cycles as anode materials in NIBs. CMK-3, a kind of ordered tubular mesoporous carbon with a pore size of about 3.9 nm, can be used as the matrix to accommodate red P and facilitate diffusion of Li^+/Na^+. Li et al. have employed the VCC method to uniformly confine red P nanoparticles in a porous carbon matrix of CMK-3 to form P@CMK-3 composites (Figure 4b).[17] The ordered mesoporous channels ensure the spatial expansion of nanored P and suppress agglomeration to enable fast Li^+/Na^+ storage. The P@CMK-3 composite exhibits a high reversible capacity of about 2250 mAh g^{-1} and enhanced cycling of 1150 mAh g^{-1} at 5 C after 1000 cycles as anodes in LIBs. These studies show that the introduction of red P into nanopores can reduce the size of the active materials, expedite the kinetics of the red P anode, and improve the cyclic stability. To further improve the properties of red P anodes, the porous structure of the carbon host should be optimized to increase the concentration of red P.

Metal-organic frameworks (MOFs) are a kind of coordination polymers developed recently. MOFs have a 3D porous structure usually with metal ions as attachment points supported by organic ligands forming 3D extensions in space. The zeolitic imidazole framework 8 (ZIF-8) is a typical MOF with a large N concentration which can be used to prepare high-quality N-doped microporous materials by carbonization and pickling treatment for catalysis and energy storage. After carbonization and pickling, high-quality N-doped microporous carbon is prepared. Li et al. have improved Na^+ storage of red P by confining amorphous red P in a ZIF-8 derived N-doped microporous carbon matrix (P@N-MPC) (Figure 4c).[56] The microporous structure of ZIF-8 derived carbon accommodates the red P nanoparticles, promotes transfer of electrons, and relieves volume expansion of red P during electrochemical sodiation/desodiation. The P@N-MPC composite anode has high reversible capacities of 600 mAh g^{-1} at 0.15 A g^{-1} after 100 cycles and 450 mAh g^{-1} at 1 A g^{-1} after 1000 cycles. The MOFs with a controllable pore structure is a promising host for red P anodes for AIBs.

The graphene aerogel matrix is 3D graphene with excellent properties such as the electrical conductivity, superelasticity, large specific surface area, and high porosity and can be used as the matrix to improve the electrochemical properties of red P anodes. Yan et al. have prepared 3D CRP-rGA nanocomposites by loading dispersed crystalline red P nanorods (CRP) into the reduced graphene oxide aerogel (rGA) matrix with molten salts by freeze-drying, and vapor redistribution (Figure 4d).[57] The CRP is uniformly distributed in the 3D rGA thus avoiding

© 2022 Wiley-VCH GmbH

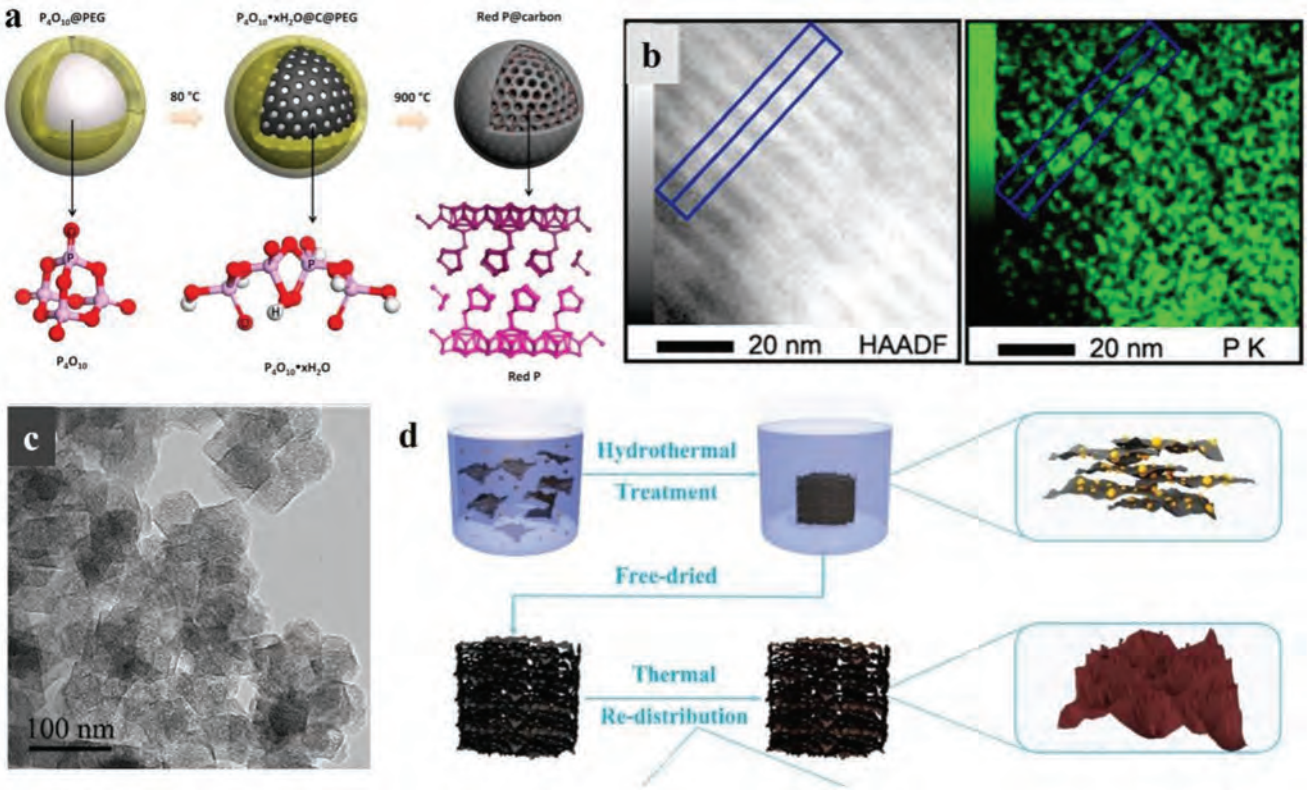

Figure 4. a) Schematic of the synthesis of ultrafine red P particles embedded in a 3D carbon framework (P/C composite). Reproduced with permission.[55] Copyright 2016, Elsevier. b) High-angle annular dark-field STEM image and P elemental map of P@CMK-3. Reproduced with permission.[17] Copyright 2016, American Chemical Society. c) TEM image of P@N-MPC. Reproduced with permission.[56] Copyright 2017, Wiley. d) Schematic illustration of the synthesis of CRP-rGA. Reproduced with permission.[57] Copyright 2017, Wiley.

aggregation of P particles during the electrochemical process. The 3D rGA structure also provides continuous channels for Na^+ and electrons and as a result, the CRP-rGA has a high initial capacity of 2427 mAh g^{-1} (758 mAh cm^{-3}) and ICE of 81.8% used as an anode in NIBs.

2.2. Black P

Black P has attracted attention in optoelectronics, biomedicine, catalysis, and energy storage applications due to its layered structure and thermodynamic stability at normal temperature and pressure.[58–64] Researchers have devised many strategies to prepare black P including the widely used high-pressure and high-temperature method,[18,65,66] high-energy mechanical milling,[67,68] and mineralizer-assisted gas-phase transformation.[69,70] These strategies have both advantages and limitations. For example, red P can be converted into black P by high-energy ball milling, but the success rate is not high due to the difficulty in controlling the temperature and pressure. In general, large-scale production of black P is still very difficult.

Alkalis react with black P to form Li_3P (or Na_3P/K_3P) in the fully discharged state thus producing a rather large theoretical specific capacity and black P has a large interlayer spacing (0.52 nm) which provides 2D interstitial space for rapid insertion/extraction of alkali metal ions ($Li^+/Na^+/K^+$).[71] Compared to red P, black P has high bulk conductivity (≈10^2 S m^{-1}), low band gap (0.34 eV), and reasonable density (2.69 g cm^{-3}), rendering it potential anode materials in AIBs. However, black P also experiences huge volume expansion in AIBs, for example, volume expansion from black P to Na_3P is as high as 499% in NIBs. Furthermore, expansion is anisotropic with rates of 3% and 92% along the *x*-axis and *y*-axis, respectively and so severe mechanical fracture and electrical contact loss can occur during charging/discharging.[72] To address the volume expansion of black P in AIBs, conductive frameworks involving carbon, metal compounds, and conductive polymers have been developed to host black P.

2.2.1. 1D Structures

CNTs provide a conductive network for black P to alleviate the volume change during electrochemical cycling due to the unique 1D structure, low resistivity, and good mechanical properties. The electrochemical characteristics of black P-CNTs composites prepared by simple mechanical mixing are not ideal because the electrical contact between the P particles and carbon matrix is limited. In addition, owing to the poor interactions between the binder and active materials, it is difficult to avoid pulverization and electrode/electrolyte interface reactions during electrochemical cycling. Haghighat-Shishavan et al. have reported a composite consisting of black P and multilayered carbon nanotubes (black P-CNTs) prepared by a

 © 2022 Wiley-VCH GmbH

surface oxidation-assisted chemical bonding process.[73] Using the Na carboxymethylcellulose-polyacrylic acid (NaCMC-PAA) binary polymer as the binder, the black P-CNTs composite is fabricated into anodes for LIBs and NIBs. Controlled air exposure enhances the hydrophilicity of black P powders producing strong bonds with the hydroxyl groups of NaCMC and carboxylic acid groups of PAA. Two types of strong bonds (P—O—C bonds and dehydration crosslinks) are formed in the materials (**Figure 5**a) and the materials have excellent electrochemical characteristics in LIBs, for instance, a high initial discharge capacity of 1345 mAh g^{-1}, capacity retention rate of 87.5% after 400 cycles and in NIBs, a high initial discharge capacity of 2073 mAh g^{-1} at 0.52 A g^{-1} and capacity retention of 75.3% after 200 cycles. Surface oxidation-assisted chemical bonding of black P with CNTs is an economical method, which provides information about the synthesis of black P-based materials and their application to energy storage.

Polypyrrole (PPy) is a heterocyclic conjugated conductive polymer with high electrical conductivity and good environmental stability and often used to modify electrode materials because it plays an important role in buffering the volume expansion, improving the electrical conductivity, and maintaining the integrity of the active materials. Sun et al. have prepared black P-CNT composites by ball milling and the black P/CNT@PPy composite is prepared by in situ polymerization of PPy.[74] The black P/CNT@PPy composite shows a reversible capacity of 1376.3 mAh g^{-1} after 200 cycles at 0.26 A g^{-1} as anodes in LIBs, which is much higher than that of the black P/CNT electrode (530.1 mAh g^{-1}) (Figure 5b). The improved electrochemical performance of P/CNT@PPy is due to the introduction of CNTs, which can partially buffer the volume expansion of black P during electrochemical cycling and improve the electrical conductivity of the material.[74] The conductive and flexible PPy coating further improves the electrical conductivity of the electrode and inhibit the side reaction between black P and the electrolyte. Moreover, PPy has strong chemisorption effects on Li_xP thereby reducing the dissolution loss of Li_xP and capacity loss during electrochemical cycling (Figure 5c).

The lack of close contact and structural cracking between active materials inevitably reduces the overall conductivity of the electrode. Zhang et al. have self-assembled black P on CNTs by chemical cross-linking.[75] These acidified CNTs are activated with a nitrogen source and bulk black P is prepared by high-energy mechanical milling. Both of them have abundant surface functional groups. During ultrasonic and magnetic stirring, the two materials attract each other via van der Waals force to form the stable hybrid (BP@CNTs) (Figure 5d). The CNTs with abundant oxygen/nitrogen functional groups provide a scaffold to anchor black P and therefore, the materials have good structural stability and high electrical conductivity because of the good mechanical properties and high electrical

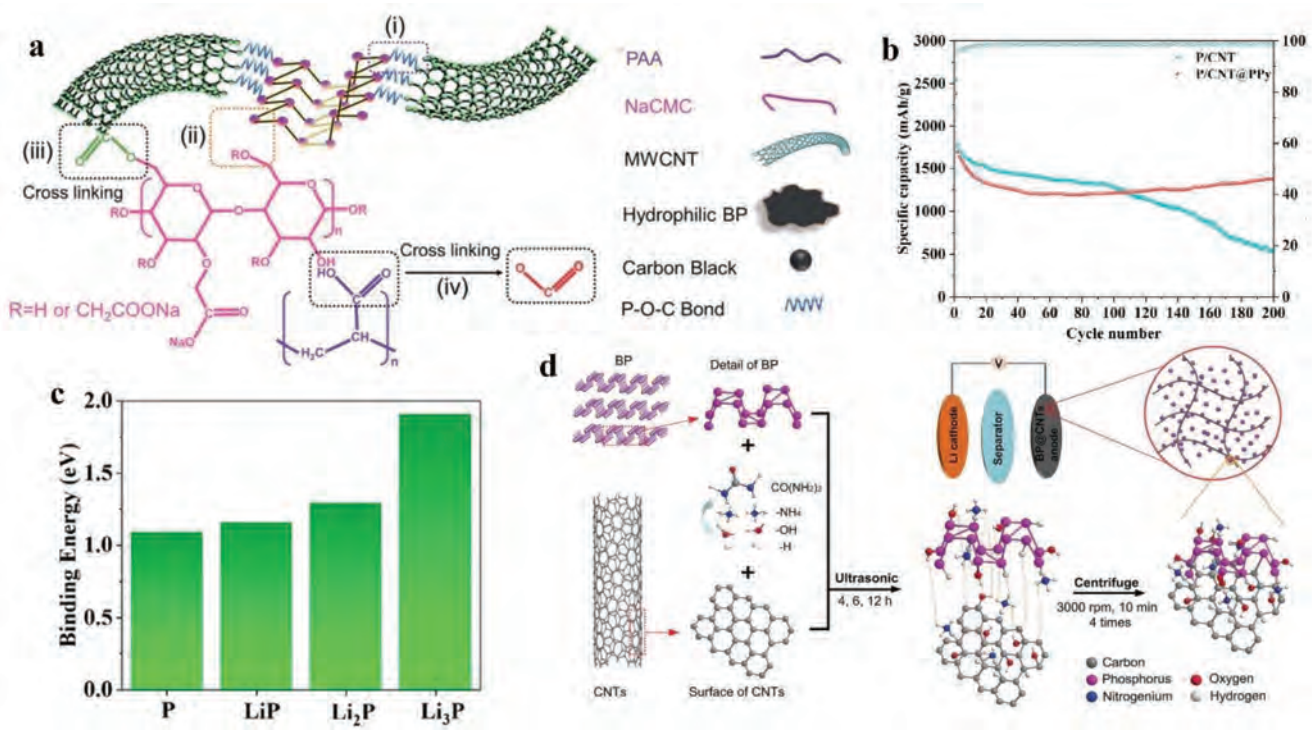

Figure 5. a) All possible types of P—O—C chemical bonds and dehydration cross-links formed between different electrode components: (i) between the hydrophilic, defective BP and functionalized CNTs, (ii) between the BP and two cross-linked binders, (iii) between the functionalized CNTs and binders formed through a dehydration reaction. The binders can also be connected during the same dehydration process, as highlighted in (iv). Reproduced with permission.[73] Copyright 2018, Royal Society of Chemistry. b) Cycling characteristics of BP/CNT@PPy and BP/CNT composites at a current density of 0.26 A g^{-1}. Reproduced with permission.[74] Copyright 2021, American Chemical Society. c) DFT-calculated binding energies of Li_xPs and PPy. Reproduced with permission.[74] Copyright 2021, American Chemical Society. d) Schematic of the synthesis of BP@CNTs hybrid and application to LIBs. Reproduced with permission.[75] Copyright 2020, Wiley.

 © 2022 Wiley-VCH GmbH

conductivity of CNTs. Consequently, BP@CNTs show good long-term cyclic stability with a high capacity of 757.3 mAh g^{-1} at 0.5 A g^{-1} after 650 cycles and high capacity of 552 mAh g^{-1} at 2.5 A g^{-1}. This study reveals that the chemical crosslinking method for self-assembly of black P on CNTs facilitates the design and fabrication of high-performance P-based anode materials for flexible and wearable ESDs.

2.2.2. 2D Structures

When graphene is combined with black P, the excellent properties such as the large specific surface area, high electrical conductivity, and good mechanical properties enable good mechanical support for black P to buffer the volume change of black P and improve the long-term cyclic stability. Liu et al. have synthesized black P/RGO hybrid materials by a simple solvothermal reaction and modified the materials with graphene stacks to prepare sandwich-structure anode films for LIBs.[76] In the solvothermal process, GO is reduced to RGO and connects to black P via P—O—C and P—C bonds (**Figure 6**a). The composite electrode has a high reversible capacity of 1401 mAh g^{-1} after 200 cycles at a current density of 0.1 A g^{-1}. Liu et al. have assembled thin films (P loading ≈78.3%) with a layered structure by filtering the red P/rGO precursors.[18] The red P is converted to black P by a high pressure treatment at room temperature (8 GPa) and the layered black P/graphene composite (black P/rGO) is produced (Figure 6b). The high activity of black P and electrical conductivity of the graphene network improve the ion/electron transfer kinetics during charging and discharging. The graphene network also provides strong mechanical support to relieve the volume change so that the

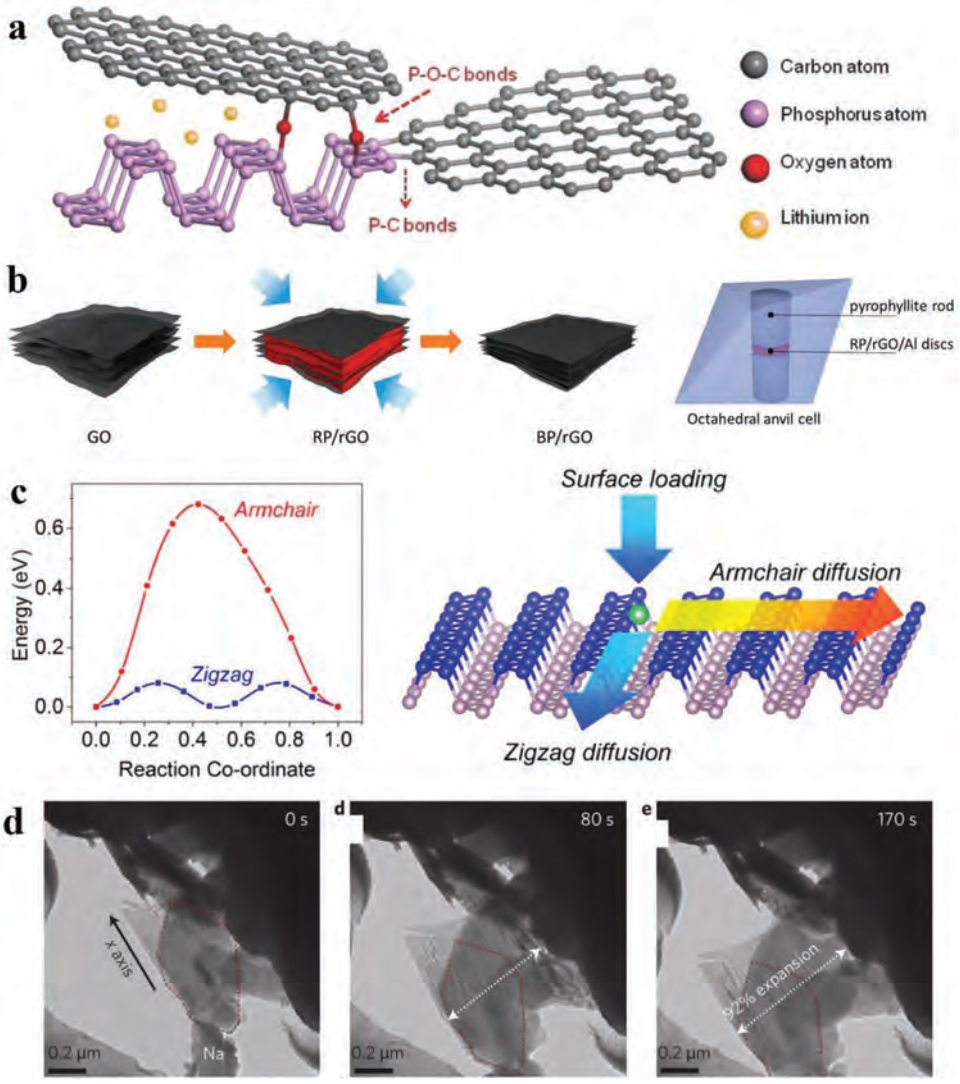

Figure 6. a) Schematic of P—C bonds and P—O—C bonds in solvothermal BPGO and storage of Li^+. Reproduced with permission.[76] Copyright 2017, Wiley. b) Schematic description of synthesis of BP/rGO. Reproduced with permission.[18] Copyright 2018, American Chemical Society. c) Energy profiles of Li diffusion along the armchair and zigzag directions on the phosphorene surface and schematic diagram of Li surface loading (adsorption process). Reproduced with permission.[24] Copyright 2015, American Chemical Society. d) Time-lapse TEM images of sodiation of black P. Na^+ traverses along the *x*-axis channel causing volume expansion along the *y*-axis. Reproduced with permission.[72] Copyright 2015, Springer Nature.

 © 2022 Wiley-VCH GmbH

black P/rGO anode has reversible capacities of 1250 mAh g^{-1} and 640 mAh g^{-1} after 500 cycles at current densities of 1 and 40 A g^{-1}, respectively, in NIBs. This simple pressurized strategy without addition of carbon black and binder is promising for the preparation of high-performance black P electrodes for AIBs.

In addition to graphene, MXene materials are considered ideal 2D supports for black P due to the excellent mechanical properties, metallic conductivity, unique in-plane anisotropic structure, and easy of surface modification.[77,78] As a representative member of MXenes, Ti_3C_2 nanosheets (TNS) have a large surface area and high electrical conductivity to facilitate electron transfer and relieve the expansion stress of black P. Meng et al. have prepared black P quantum dots (BPQD)/Ti_3C_2 nanosheet (TNS) composites by ultrasonic and freeze-drying treatments.[79] The atomic charge of the BPQD/TNS composites is calculated using Bader's charge group analysis. The calculated results show that the charge of the p-orbital of the P atom is transferred to the p-orbital of the O and surface Ti ions through the P—O—Ti interfacial bond. At the same time, the charge of the inner Ti ions is transferred from their d orbitals to the surface Ti ions through C atoms. The atomic charge polarization induced by P—O—Ti interfacial bonds enhances the charge adsorption and efficient interfacial electron transfer, thus providing fast energy storage.[79] Therefore, the combination of BPQD and TNS via strong interfacial covalent bonds (Ti-O-P) improves the conductivity of black P and alleviates the expansion stress during electrochemical cycling. The BPQD/Ti_3C_2 anode in LIBs shows a high reversible capacity of 910 mAh g^{-1} at 0.1 A g^{-1} and long-cyclic stability of over 100% capacity retention at 1 A g^{-1} for 2400 cycles. This work exploits the surface chemistry of 2D materials to anchor black P nanoparticles by interfacial assembly and shows great potential in the preparation of advanced AIBs materials.

Phosphorene, a wrinkled 2D structure that can be prepared from bulk black P by mechanical exfoliation or liquid phase exfoliation, is very promising as anode materials in AIBs due to the fast and directional diffusion channels for Li^+/Na^+.[80–82] Density-functional theory (DFT) calculation shows that the wrinkled structure of phosphorene enables migration of Li^+ and Na^+ anisotropically (more favorable in the zigzag direction) and the low diffusion barrier along the zigzag direction leads to high diffusion rates (Figure 6c).[23,24] The diffusion rate of Li^+ in the zigzag direction of phosphorene is estimated to be 1.4×10^4 times larger than that on graphene at room temperature. The high diffusivity of Li^+ on phosphorene produces the fast charging/discharging capability for LIBs and besides the small diffusion barrier, LIBs with phosphorene-based anodes provide a large charging voltage (2.9 V).[24] Therefore, phosphorene-based LIBs have broad application prospects.

The Na adsorption energy on phosphorene is larger than the Na binding energy and Na volume cohesion energy in the Na dimer, indicating that Na atoms do not aggregate at small Na concentrations. The monolayer phosphorene has high theoretical specific capacities (NaP: 865 mAh g^{-1} and NaP_2: 433 mAh g^{-1}) and after Na insertion, phosphorene has high mechanical stability and integrity. Na-P also has metallic properties at high Na concentrations and the electrical conductivity is better than that of amorphous red P phase boding well for Na^+ storage at high currents.[23] Sun et al. have observed potentiostatic sodiation of black P particles by in situ TEM and found that the expansion rates of black P along the *x*-axis and *y*-axis are 0 and 92%, respectively (Figure 6d).[72] Based on the theory that the volume expansion of black P into Na_3P is about 500%, it is speculated that a significant expansion of 160% occurs along the *z*-axis and minimizing the width and thickness of the black P layer helps reduce the stress buildup along the *y*- and *z*-axes. Therefore, electrodes with a single layer of black P (phosphorene) are proposed and to further reduce the expansion stress, phosphorene is sandwiched between graphene. The phosphorene composite shows a high reversible specific capacity of 2440 mAh g^{-1} at 0.05 A g^{-1} and retention of 83% after 100 cycles (83% after 100 cycles) as anodes in NIBs.[72] In the composite, graphene improves the electrical conductivity and provides an elastic buffer when the phosphorene is alloyed to form Na_3P to alleviate expansion along the *Y* and *Z* axes. Zhang et al. have reported the preparation of densely packed phosphorene–graphene composites (PG-SPS) by liquid phase exfoliation and spark plasma sintering.[83] The PG-SPS exhibits good rate capability (415.0 mAh g^{-1} at 10 A g^{-1}) and cyclic performance (91.9% retention after 800 cycles at 10 A g^{-1}) as anodes in LIBs. The ICE of the PG-SPS electrode (60.2%) is higher than that of the bare phosphorene electrode (11.5%) and the loosely stacked phosphorene–graphene (34.3%) electrode due to the good electrical contact between reduced GO and black P. This work uses liquid phase exfoliation and spark plasma sintering to prepare phosphorene to overcome the difficulties of large-scale fabrication and poor air stability.

Another strategy to improve Na^+ storage of phosphorene is to compound phosphorene with MXene to form heterostructures of 2D stacks. Guo et al. have prepared hybrid anodes of phosphorene/MXene by self-assembly for stable and fast storage of Na^+.[84] The $Ti_3C_2T_x$ MXene with sufficient surface functional groups and high mechanical strength can provide a 2D constrained environment for recombination of phosphorenes to relieve structural expansion and pulverization during electrochemical cycling. DFT calculation confirms that the Na affinity and diffusion kinetics in the phosphorene/MXene heterostructure are significantly enhanced and X-ray photoelectron spectroscopy shows that fluorine terminations of MXene produce a stable solid electrolyte by forming a fluorine-rich compound on the anode surface. The phosphorene/MXene composite anode shows a high reversible capacity of 535 mAh g^{-1} at 0.1 A g^{-1} and 87% capacity retention after 1000 cycles. This work reveals the regulation strategy of 2D materials with functional groups on the phosphorene anode SEI to improve the electrochemical performance of AIBs.

2.2.3. 3D Structures

High-energy ball milling is a simple method to compound black P with carbon materials. Park et al. have used amorphous red P and graphite as starting materials to prepare black P nanoparticle–graphite composites by the mechanochemical reaction during high-energy mechanical milling.[67] Stable P—C bonds are formed in the black P nanoparticle-graphite composite (**Figure 7**a) and remain stable during lithiation/delithiation

 © 2022 Wiley-VCH GmbH

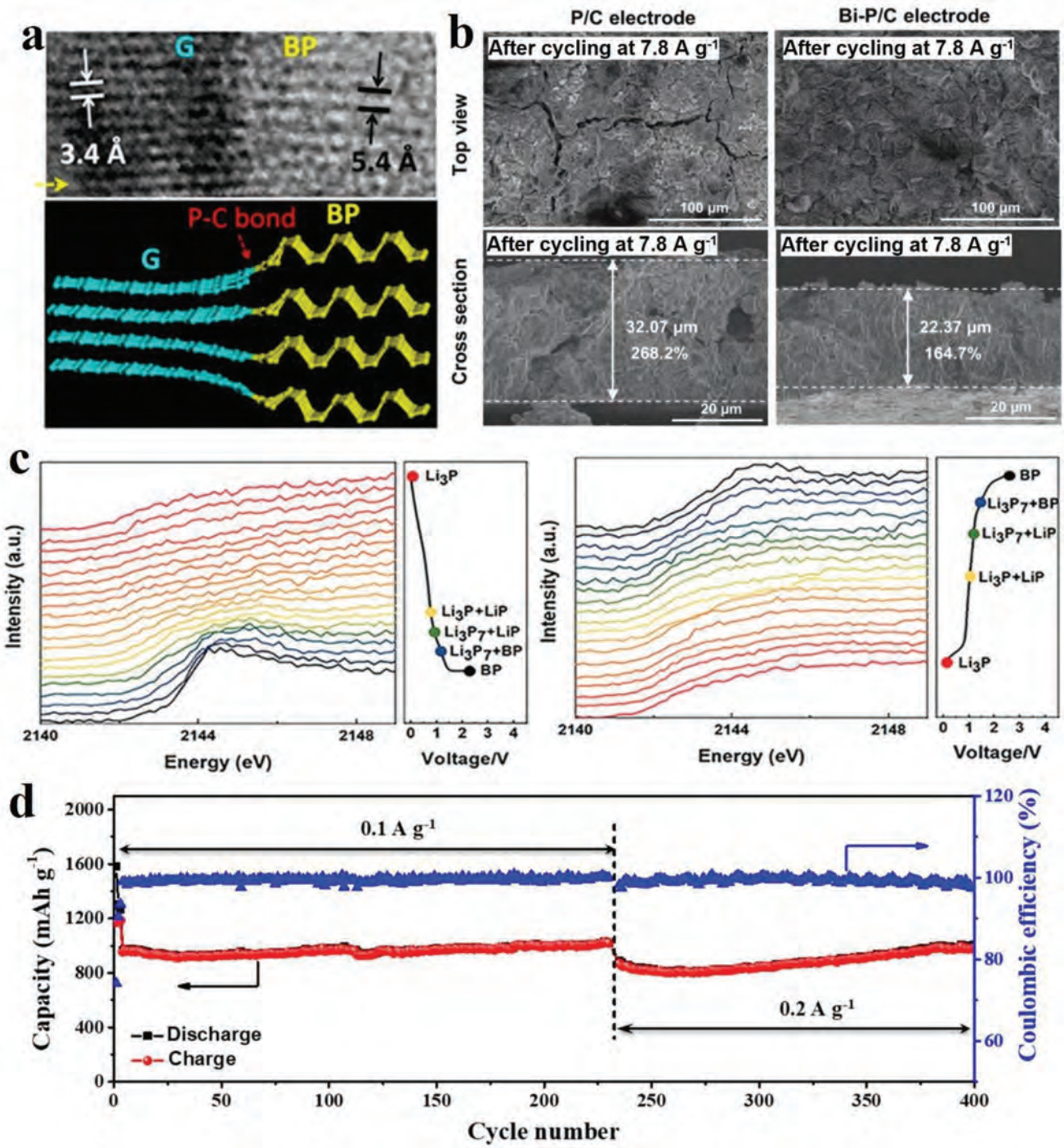

Figure 7. a) HR-TEM image and schematic of the BP-G composite. Reproduced with permission.[67] Copyright 2007, Wiley. b) SEM images of top-view and cross-sectional morphologies of P/C and Bi-P/C electrodes after 300 cycles at 7.8 A g^{-1}. Reproduced with permission.[88] Copyright 2022, Wiley. c) Operando XRD spectra of the BP/G/CNTs electrode during charging/discharging. Reproduced with permission.[87] Copyright 2021, Wiley. d) Cycling characteristics of the Li/BP@NC electrode. Reproduced with permission.[89] Copyright 2021, American Chemical Society.

thus preventing damage of the black P/carbon structure during cycling and maintaining good electron conduction between P and carbon.[85] Peng et al. have prepared a low-cost black P-carbon nanocomposite by long-term ball milling of commercial red P and super P carbon black.[86] The black P nanodomains are embedded in the amorphous carbon matrix to form a tightly bound 3D structure with good electrical conductivity and stability during electrochemical cycling. The composite has a high reversible capacity of 1381 mAh g^{-1} after 100 cycles (≈90.5% of the initial reversible capacity) as anodes in LIBs. Li et al. have prepared a composite with nanoscale black P, graphite, and carbon nanotubes (BP/G/CNTs) by planetary ball milling

 © 2022 Wiley-VCH GmbH

for anodes in LIBs.[87] The BP/G/CNTs anode has high reversible capacities of 1031.7 mAh g^{-1} after 450 cycles at 0.15 A g^{-1} and 508.1 mAh g^{-1} after 3000 cycles at 2 A g^{-1}. The reaction between black P and Li^+ during the electrochemical process forms Li_3P_7, LiP, and Li_3P and the corresponding formation potentials are studied by ex situ and in situ synchrotron techniques. During discharging, black P is converted into Li_3P_7, LiP, and Li_3P at 1.119, 0.925, and 0.788 V, respectively (Figure 7c) and the complete transition from black P to Li_3P is completed at 0.001 V. During charging, Li_3P is converted into LiP, Li_3P_7, and P at 1.028, 1.233, and 1.599 V, respectively.

In addition to carbon materials, ball milling with metal materials is an effective strategy to improve the electrochemical properties of P anodes. Zhang et al. have synthesized Bi-P/C composites by ball milling of bismuth (Bi), P, and graphite.[88] Bi has a low Li^+ diffusion barrier and high electrical conductivity and its electrochemical kinetics is better than that of P. The lithiation potential is also higher than that of P anode, while the delithiation potential is lower than that of the P anode. At a large current density, Bi plays the role of a "Li reservoir" to promote uniform distributions of Li in the P particles to reduce the structural stress caused by volume expansion of P during lithiation as well as volume expansion of the entire electrode (Figure 7b), thus improving the fast charging characteristics. The P–Bi interface shows strong chemisorption to capture soluble polyphosphides during rapid charging and significantly improve the long cyclic stability. The Bi–P/C anode has excellent electrochemical properties as exemplified by a high specific capacity of 1788.2 mAh g^{-1} at a current density of 13 A g^{-1} and capacity retention of 86.3% after 300 cycles at 7.8 A g^{-1}. This "Li reservoir" provides a new solution for charging and discharging of P anode materials at high current densities.

Black P can be also combined with long-chain polymers to produce flexible thin-film electrodes. Wang et al. have fabricated a free-standing flexible anode (BP@NC) composed of black P nanosheets and nanocellulose by a simple vacuum-assisted filtration method.[89] Substrate elongation of the nanocellulose films is up to 10.2% to relieve the volume expansion of the black P electrode during electrochemical cycling. Theoretical calculation shows that the repulsive force of Li^+ at the interface between black P and nanocellulose in the BP@NC layer is smaller than that of the black P interlayer or single black P layer, thereby being beneficial to the reaction kinetics. The BP@NC composite has a high reversible capacity of 994.4 mAh g^{-1} after 400 cycles at 0.2 A g^{-1} together with a high capacity retention rate of 84.9% (Figure 7d). This study suggests the use of long-chain polymers such as the low-cost cellulose to construct flexible black P anodes for high-performance AIBs.

2.3. Metal phosphides

Metal phosphides have been studied as promising anode materials in AIBs on account of the good electrical conductivity, high theoretical capacity, and suitable redox potential.[27] The electrochemical reactions between metal phosphides and alkali ions (e.g., Li^+, Na^+, and K^+) generally include the following three types (Equations 1–3), namely, interaction, conversion, and alloying[90]:

(1) Intercalation reaction:

$$M_xP_y + zLi^+\left(Na^+, K^+\right) + ze^- \leftrightarrow Li(Na,K)_z M_xP_y \quad (1)$$

(2) Conversion reaction:

$$M_xP_y + 3yLi^+\left(Na^+, K^+\right) + 3ye^- \leftrightarrow yLi(Na,K)_3 P_3 + xM \quad (2)$$

(3) Alloying reaction:

$$xM + zLi^+\left(Na^+, K^+\right) + ze^- \leftrightarrow Li(Na,K)_z M_x \quad (3)$$

Therefore, the electrochemical mechanism of metal phosphide anodes is more complicated than that of P anodes. $Li_zM_xP_y$ is formed by intercalation of metal phosphides (e.g., MnP_4, VP, and VP_4), which have a stable crystal structure.[9] If metal phosphides do not have a stable crystal structure, the structure collapses after multiple insertion/extraction via the conversion reaction, and the bonds between the metal and P break to form nanoscale Li_3P and M. If the precipitated metal is reactive with alkali ions, Li_xM is formed by the reversible alloying process.

In general, metal phosphides store Li^+, Na^+, or K^+ by the transformation (and alloying) mechanisms and have large gravimetric and volumetric specific capacities. Metal phosphides also have high electrical conductivity because the metal atoms provide channels for electrons to yield high utilization.[30] However, metal phosphides as anode materials for AIBs face challenges, such as the severe volume expansion during the electrochemical cycling leads to the pulverization and rapid capacity fading of electrode materials. Take the sodiation/desodiation process of Sn_4P_3 as an example. The volume expansion of P to Na_3P and Sn to $Na_{15}Sn_4$ is 490% and 525%, which seriously affects the electrochemical stability of the Sn_4P_3 electrode.[27] Furthermore, the ion diffusion kinetics of metal phosphides is slow, limiting their ability to charge and discharge at high current density. Li et al. have improved the reaction kinetics of metal phosphide by designing the structure of N-doped carbon-coated FeP (FeP@NC).[91] The calculated Li^+ diffusion coefficients of FeP@NC and bare FeP are 2.49×10^{-11} and 2.12×10^{-11} cm^2 s^{-1}, respectively.[91] The improved reaction kinetics of FeP@NC is due to the porous nanosheets structure that can shorten the migration path of ions and increase the contact area between the electrode and the electrolyte. In addition, the conductive N-doped carbon coating layer provides a channel for the rapid electron transport. To solve these problems, researchers have designed and studied a variety of nano and microstructures which provide sufficient space for volume expansion, increase the contact area between the electrolyte and active materials, promote diffusion of alkali ions, and improve the electrochemical performance.

2.3.1. 1D Structures

Metal phosphide anode materials with 1D nanostructures such as nanofibers, nanotubes, and nanowires have attracted

 © 2022 Wiley-VCH GmbH

extensive attention as these unique 1D nanostructures can shorten the transportation paths of ions and electrons, alleviate agglomeration of the active particles, and accommodate the volume expansion of metal phosphides.

Metal phosphide has good electrical conductivity, and the metal phosphide nanowires prepared by the bottom-up method have a large aspect ratio, which can construct a self-supporting conductive network without the need for composite with carbon materials to further improve the electrical conductivity. In addition, after the metal phosphide is nanosized, there is enough space to buffer its volume expansion during the charging and discharging process. Therefore, pure metal phosphide nanowires do not need to be combined with carbon materials, thus avoiding the addition of inactive substances and the electrodes typically have high gravimetric specific capacity. Li et al. have synthesized high-quality and high-yield CuP_2 nanowires by supercritical fluid-liquid-solid (SFLS) growth.[19] The CuP_2 nanowires have a high aspect ratio (32.5 ± 2.3 nm in diameter and length of several tens of micrometers) entangled with each other. As anode materials in LIBs, the binder-free CuP_2 nanowire electrodes have good electrochemical cycling properties (88% capacity after 100 cycles at 0.1 A g^{-1}), rates (high reversible capacity of 600 mAh g^{-1} at 6 A g^{-1}), high initial discharge capacity of 1075 mAh g^{-1}, and 88% capacity retention after 100 cycles at 0.1 A g^{-1}. Even after cycling at a high rate of 6 A g^{-1}, the electrode shows a high reversible capacity of 600 mAh g^{-1}. The excellent electrochemical properties stem from the large aspect ratio of the nanowires, large buffering space for expansion of CuP_2, and short transportation distance for Li^+. Li et al. have prepared self-supported Zn_3P_2 nanowire bundles on the titanium foil by chemical vapor deposition.[92] The Zn_3P_2 nanowires have the shape of sea urchin balls with a large active surface area and short diffusion distance for Li^+ as anode materials in LIBs and NIBs (**Figure 8**a). In the absence of conductive additives and conventional binders, the Zn_3P_2 anode has high rates for storage of Li^+ (high reversible capacity of 350 mAh g^{-1} at a high current density of 40 A g^{-1}) and Na^+ (a high rate capacity of 280 mAh g^{-1} at 5 A g^{-1}). This assembly method taking advantage of the inherent properties of nanowires simplifies the preparation process of traditional

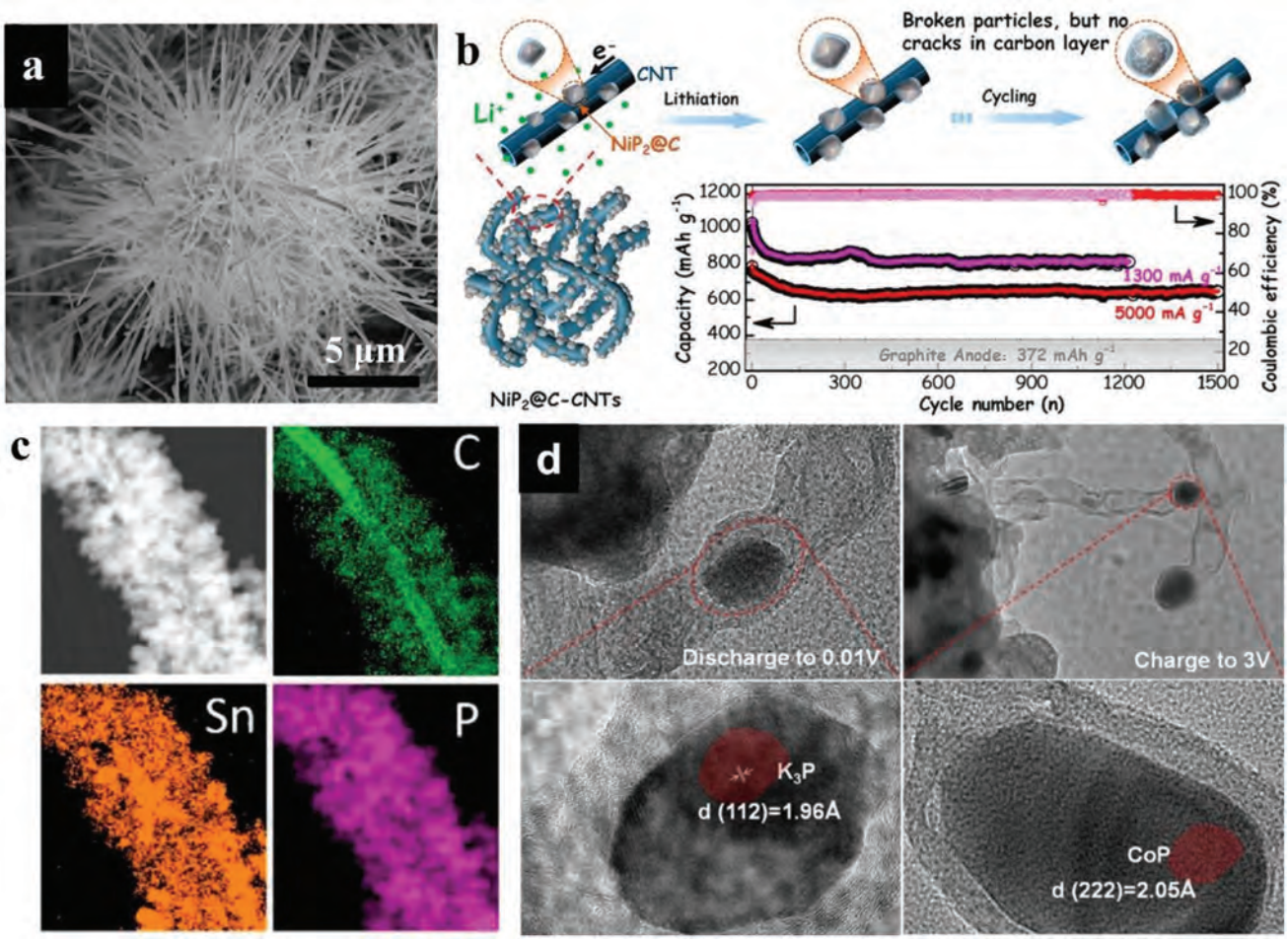

Figure 8. a) High-magnification SEM image of the Zn_3P_2 nanowire-assembled bundle/titanium foil integrated anode. Reproduced with permission.[92] Copyright 2017, Elsevier. b) Schematic of the synthesis and long-term cycling properties of the NiP_2@C-CNTs nanocomposite. Reproduced with permission.[93] Copyright 2017, American Chemical Society. c) EDS maps of $Sn4P_3$@CNT/C. Reproduced with permission.[94] Copyright 2020, American Chemical Society. d) Ex-TEM images of the cycled AC@CoP/NCNTs/CNFs electrode in KIB at different potentials. Reproduced with permission.[95] Copyright 2019, Elsevier.

 © 2022 Wiley-VCH GmbH

electrodes and provides more possibilities for the preparation of high-energy-density AIBs based on metal phosphine-based anode materials.

Structural collapse of metal phosphine-based anodes due to the large volume expansion during electrochemical cycling remains a major challenge and limiting metal phosphate nanoparticles in flexible conductive matrices such as CNTs and CNFs can overcome the hurdle while maintaining the monodispersed properties of electrically active particles in the matrix. Luo et al. have synthesized monodispersed carbon-coated cubic NiP_2 nanoparticles and fixed them on CNTs (NiP_2@C-CNTs).[93] The thickness of the carbon layer is about 3 nm and it prevents NiP_2 particles from agglomeration to provide good electrical contact (Figure 8b). NiP_2@C-CNTs exhibit excellent electrochemical cyclic stability with high reversible capacities of 816 mAh g^{-1} after 1200 cycles at 0.13 A g^{-1} and 654.5 mAh g^{-1} after 1500 cycles at 5 A g^{-1} for storage of Li^+. This strategy is also applicable to metal phosphides in NIBs. Ran et al. have fabricated a Sn_4P_3 heterostructure (Sn_4P_3@CNT/C) on CNT by a hydrothermal reaction and thermal treatment.[94] This structure resembles a bottle brush in which the CNTs provide fast electron transportation and mechanical support (Figure 8c). The nanoscale Sn_4P_3 particles are attached to the surface of CNTs to increase the contact area between the Sn_4P_3 particles and electrolyte and shorten the diffusion distance for ions. The amorphous carbon coating on Sn_4P_3 buffers the volume change during electrochemical cycling and the Sn_4P_3@CNT/C anode delivers excellent electrochemical performance (449 mAh g^{-1} after 500 cycles at 2 A g^{-1}) in NIBs. One of the keys is to confine the nanoscale active materials in the flexible carbon matrix such as CNTs to prevent agglomeration.

MOFs are composed of metals and organic ligands forming the carbon-coated metal phosphide structures in situ upon carbonization and phosphating. Miao et al. have utilized electrospinning of ZIF to prepare ZIF-67/ZIF-8 derived N-doped carbon nanotubes (NCNTs) on CNFs.[95] The Co particles in the metal-organic framework form CNTs on the surface of CNFs, whereas Zn particles disappear after calcination to form the core framework. After subsequent oxidation and phosphating, the special structure of AC@CoP/NCNT/CNFs of the CNT supported on the nanofibers and CoP nanoparticles embedded on top of the CNT is obtained (Figure 8d). The amorphous carbon layer outside the CoP particles acts as a shell to inhibit volume expansion of the active materials during charging/discharging. The N-doped CNFs also provide a continuous network for electron transport and the AC@CoP/NCNT/CNFs nanocomposite anode has a high reversible capacity of 247 mAh g^{-1} after 1000 cycles at 0.8 A g^{-1} in KIBs. The unique structure of AC@CoP/NCNTs/CNFs provides excellent cyclic stability but because of the large proportion of carbon skeletons, the specific capacity is low but it can be optimized.

2.3.2. 2D Structures

Owing to confinement of carrier migration and heat diffusion in the 2D plane, 2D materials have good optical properties, high thermal conductivity, and electrical conductivity. When 2D materials are arranged orderly, the large surface area provides ample active sites and shortens the diffusion distance for ions boding well for the high capacity and fast charging/discharging. Therefore, metal phosphides with the 2D structure are promising anode materials in AIBs.

One of the main reasons for the degraded battery performance is that the electrode may undergo irreversible structural changes after repetitive charging and discharging. Li et al. have found that the initial layered crystal structure of GeP can be reconstructed during charging due to its small formation energy thus providing electrochemical reversibility.[96] A 2D self-healing GeP/C anode with a layered structure has been synthesized by a two-step ball milling and low-temperature annealing process.[96] The GeP/C composite electrode shows a high reversible capacity exceeding 1750 mAh g^{-1} after 600 cycles at a current density of 0.2 A g^{-1}. Even at a high current density of 5 A g^{-1}, the capacity retention is still as high as 63%. The excellent electrochemical performance of the GeP/C composite is attributed to the layered crystal structure of GeP that can be reconfigured during electrochemical cycling in conjunction with the high Li^+ conductivity of the intercalated Li_xGeP. The small size of the carbon matrix and GeP particles promotes penetration of the electrolyte, shortens the diffusion length of Li^+, and improves the reaction kinetics.

Owing to the high surface energy, 2D nanomaterials have a strong tendency to aggregate, resulting in loss of active sites and blockage of ion transportation pathways. Coating 2D metal phosphides with carbon or anchoring with a supporting framework is an effective way to tackle this challenge. Han et al. have prepared dispersed porous carbon-coated FeP nanosheets (FeP@C) by combining the hydrothermal reaction, carbon coating process, and phosphating treatment.[97] With enough space between adjacent plates, the continuous carbon layer maintains the mechanical integrity and the plate-like nanostructures have shorter electron/ion transport paths and can accommodate the large volume changes of FeP during Li intercalation and deintercalation. The FeP@C anode shows excellent cycling characteristics (610 mAh g^{-1} after 400 cycles at 0.5 A g^{-1}) and rates (347 mAh g^{-1} at a high current density of 5 A g^{-1}). This work demonstrates that the plate-like nanostructure, carbon coating, and internal mesoporous channels of FeP are key to improve the structural stability and Li^+ storage of metal phosphide anodes.

Graphene has been used as an additive or substrate for metal phosphides due to the good mechanical strength, toughness, and electrical conductivity.[98] For example, Cai et al. have used a two-step process involving the hydrothermal treatment and low-temperature phosphating to prepare the Ni_2P@rGO composite assembled by rose-like Ni_2P nanosheets immobilized on the rGO matrix.[99] On the one hand, the rose-shaped Ni_2P nanosheets alleviate the volume expansion in the horizontal direction during charging/discharging and shorten the transportation paths of Li^+. On the other hand, addition of rGO prevents agglomeration and accumulation of Ni_2P sheets and provides a continuous conductive network for electrons. As a result, the Ni_2P@rGO composite electrode has high reversible capacities of 200.5 mAh g^{-1} at 1 A g^{-1} and 245.8 mAh g^{-1} at 0.3 A g^{-1} after 300 cycles, respectively. Zhao et al. have synthesized monodispersed $SnP_{0.94}$ nanoplates by simple hot injection.[100] With the aid of chitosan, $SnP_{0.94}$ nanoplates are in situ encapsulated

© 2022 Wiley-VCH GmbH

by GO sheets through hydrogen bonding and electrostatic interactions to form the $SnP_{0.94}$@GO composite. As anode materials in KIBs, the $SnP_{0.94}$@GO composite provides a high reversible capacity of 106 mAh g^{-1} after 100 cycles corresponding to capacity retention of 93%. The excellent electrochemical cyclic stability of the $SnP_{0.94}$@GO electrode is ascribed to the confinement effects of GO and no obvious aggregation of $SnP_{0.94}$ particles after 100 cycles, which is in sharp contrast to severe aggregation in pure SnP.

The unique 2D layered structure of MXene provides more insertion channels for ions, making it possible to achieve rapid ion diffusion in the complex of transition metal phosphide and MXene. Wang et al. have used low-temperature phosphating to form CoP-Co_2P on the surface of Ti_3C_2 nanosheets to increase the interlayer spacing of Ti_3C_2 nanosheets and transmission efficiency of Li^+.[101] The dispersed CoP-Co_2P particles provide abundant active sites for intercalation/deintercalation of Li^+. The unique chemical stability and lamellar shape of Ti_3C_2 avoid agglomeration and pulverization of CoP-Co_2P particles to improve the electrochemical cyclic stability of the CoP-Co_2P/Ti_3C_2 electrode. The CoP-Co_2P/Ti_3C_2 electrode has a high specific capacity of 650 mAh g^{-1} after 1000 cycles at 0.7 A g^{-1}. In this work, the self-growth method of cobalt phosphide on Ti_3C_2 nanosheets is a new strategy for the preparation of MXene-metal phosphide electrodes.

2.3.3. 3D Structures

3D porous structures can be designed to optimize the various characteristics of electrode materials such as active sites, transportation paths, and volume expansion. Gao et al. have used Co–Co Prussian blue analogs as templates combined with graphene aerogel (GA) in a low-temperature phosphating process to obtain CoP@GA composites (**Figure 9**a).[102] The porous CoP nanocubes are uniformly distributed and firmly encapsulated in the 3D graphene aerogel framework. The conductive 3D framework buffers the large volume expansion of CoP during electrochemical cycling and the porous structure facilitates penetration of the electrolyte into the electrode to shorten the ion diffusion path. As anode materials in LIBs, the CoP@GA composite shows a high initial discharge capacity of 1212.9 mAh g^{-1} at 0.2 A g^{-1} with ICE of 88.6%, and a reversible capacity of 351.8 mAh g^{-1} after 4000 cycles at a high current density of 10 A g^{-1}. This work reveals a facile and economical template-based method for the synthesis of high-performance 3D metal phosphides for AIBs.

Core–shell structures are ordered combinations of one material wrapped around another by chemical bonds or other forces. Compared to single-component structures, metal phosphides with the core–shell structure have better electrochemical properties. Specifically, the carbon shell on the surface of the metal phosphide enhances the conductivity of the electrode and transfer of ions. Meanwhile, the carbon shell ensures effective growth of the SEI layer and avoids cracking and reforming of the SEI. Therefore, the electrochemical properties of core–shell electrode materials are improved. There is also extra space between the core and shell to relieve the volume expansion of the active materials and prevent the anode from pulverization during electrochemical cycling. For example, Ma et al. have synthesized GaP@C nanoparticles with the core–shell structure by chemical vapor deposition with improved electrochemical performance and structural integrity (Figure 9b).[103] The GaP@C anode exhibits a high reversible capacity of 812 mAh g^{-1} after 100 cycles at 0.5 A g^{-1} and rate performance of 1087 mAh g^{-1} at 2 A g^{-1} in LIBs. Liang et al. have used metal hydroxide and glucose as precursors to generate Ni_2P@C with the core–shell structure in situ in a PH_3/He plasma environment.[104] This

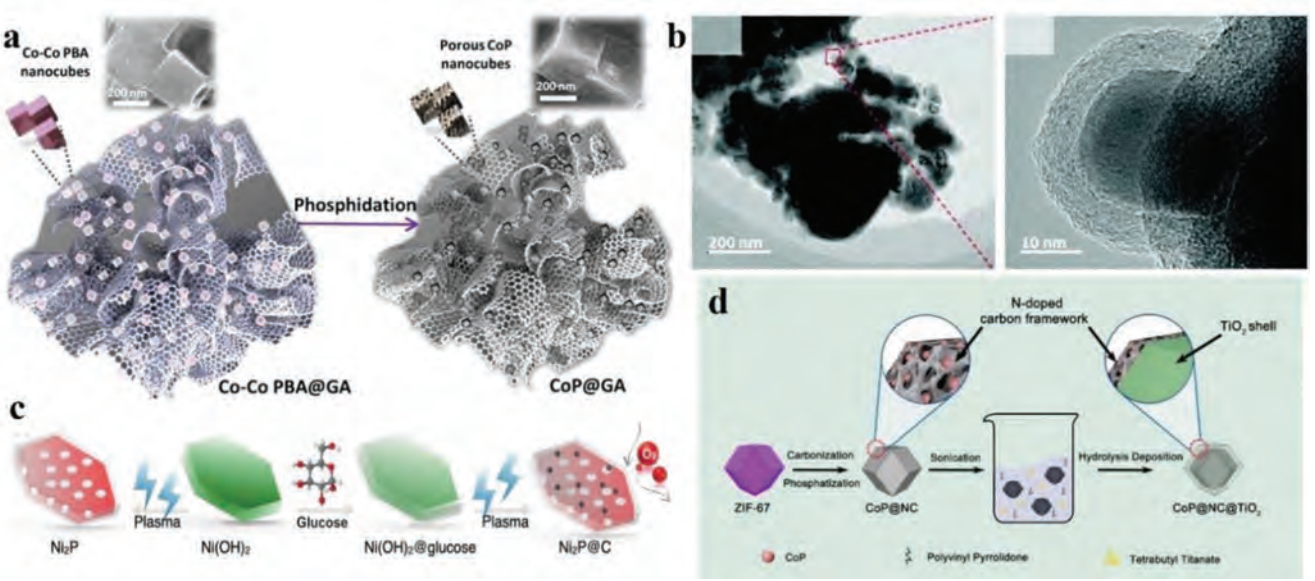

Figure 9. a) Schematic illustration of the fabrication of the CoP@GA composite. Reproduced with permission.[102] Copyright 2019, American Chemical Society. b) TEM images of the pristine GaP@C composite. Reproduced with permission.[103] Copyright 2021, Royal Society of Chemistry. c) Schematic illustration of the synthesis process of Ni_2P and Ni_2P@C. Reproduced with permission.[104] Copyright 2021, Springer Nature. d) Schematic illustration of the preparation of the CoP@NC@TiO_2 composite. Reproduced with permission.[105] Copyright 2021, Wiley.

 © 2022 Wiley-VCH GmbH

strategy can prevent oxidation of the phosphating materials and maintaining the high conductivity of Ni_2P. The high-energy plasma introduces a large number of defects and pores beneficial to the electrochemical reactions of Ni_2P@C (Figure 9c). As anode materials in NIBs, the Ni_2P@C shows a high capacity of 693 mAh g^{-1} after 50 cycles at a current density of 0.1 A g^{-1} and retention of 77% capacity after 1500 cycles at a high rate of 2 A g^{-1}. Chen et al. have used ZIF-67 nanoparticles as precursors and decomposed organic ligands by carbonization and phosphating to form porous N-doped carbon frameworks (CoP@NC) with a uniform distribution of CoP particles.[105] The TiO_2 is uniformly coated on the surface of CoP@NC through hydrolysis of tetrabutyl titanate to form the core–shell CoP@NC@TiO_2 composite (Figure 9d). The N-doped carbon framework derived from the ZIF-67 precursor improves the electrical conductivity of the electrode and accommodates the volume expansion of CoP particles. Besides, the TiO_2 shell buffers the mechanical stress during electrochemical cycling and maintains the integrity of the carbon framework. As anode materials in LIBs, the core–shell CoP@NC@TiO_2 composite shows a high reversible capacity of 706.3 mAh g^{-1} after 1200 cycles at 0.1 A g^{-1}. Hence, the shell–core structure is a promising universal electrode design, which can overcome the challenges of transition metal phosphide anodes in AIBs.

In this part, the advanced structural designs (1D, 2D, and 3D) of P-based anode for AIBs are discussed in depth, and the introduction of these advanced structural designs makes P-based anode (red P, black P, and metal phosphides) with improved electrochemical performance. Based on the discussion, we can see that different P-based anode structure designs can endow the P-based anode with different properties. For example, 1D structure design can shorten the ion and electron transport path, 2D structure design can provide ample active sites and shorten the diffusion distance for ions, and 3D structure design can provide robust support to buffer the large volume expansion of electrodes during the electrochemical cycling process. On the other hand, on the basis of these structural designs, further endowed with chemical bond cooperation (e.g., P—C bond, P—O—C bond, and Ti—O—P bond) between the matrix material and the active substance can better improve the interfacial stability of the P-based anode material. Therefore, the ideal P-based anode should have excellent electrical conductivity, a short ion and electron transport path, a large active surface, as many active sites as possible, and can well accommodate the volume change of electrode during electrochemical cycling. However, it should be noted that the pore volume of the electrode should not be too large because too large pore volume of the electrode will reduce the conductivity, tap density, and volumetric capacity of the electrode. Therefore, the rational porous structure design is significant to the commercial application of P-based anode.

3. P-Based Cathode Materials

Among the various cathode materials for AIBs, polyanionic materials such as phosphates ($LiMPO_4$),[106] orthosilicates (Li_2MSiO_4),[107,108] borates ($LiMBO_3$),[109] fluorophosphates ($LiM(PO_4)F$),[110,111] pyrophosphates (Li_2MP2O_7),[112,113] and tavorite fluorosulfates ($LiMSO_4F$) (M = e.g., Fe, Co, Ni, Mn, and V) have received extensive attention due to the high redox potential and good thermal stability.

Polyanionic compounds are 3D structures with strong covalent bonds and the stable framework has the characteristics of fast ion diffusion, small volume change, and less phase transition during ion deintercalation/intercalation for good cyclic stability and safety in LIBs and NIBs. In polyanionic materials, the M—O bond can be weakened by introducing an electronegative anion such as P, Si, and S. This decreases the splitting energy between the bonding and antibonding orbitals of the M—O bond and increases the energy difference between antibonding orbitals and the vacuum to increase the working potential.[12,114,115] Taking iron-based materials and cobalt-based materials as examples, the discharge voltages of polyanionic materials correspond to $LiFeO_2$ (2.98 V vs Li/Li^+) and $LiCoO_2$ (≈3.9 V vs Li/Li^+) are 3.5 V versus Li/Li^+ ($LiFePO_4$) and 4.8 V versus Li/Li^+ ($LiMnPO_4$), respectively.[116,117] Compared with other anions, P anions weaken the M-O bond to a greater extent to yield a higher working potential.[118] In addition, the atomic mass of P is smaller than that of S, Ge, and As being conducive to the higher specific capacity of PO_4 polyanions materials and P-based cathode materials are highly regarded for AIBs.

3.1. Phosphates

Phosphate polyanion cathode materials ($LiMPO_4$, M = Fe, Co, Ni, and Mn, for example) have the advantages of high electrochemical potential, long cyclic stability, good thermal stability, and specific capacity close to the theoretical limit. $LiFePO_4$ is one of the developed phosphate cathode materials for electric vehicles and ESDs due to the abundant raw materials, low price, relatively low toxicity, and high thermal stability.[119] $LiFePO_4$ has the olivine-type structure and the space group is *Pnmb* with structural units comprising the LiO_6 octahedron, FeO_6 octahedron, and PO_4 tetrahedron (**Figure 10**a).[120] In the *b*-axis direction, FeO_6 octahedrons are connected at a certain angle on the bc plane. The LiO_6 octahedrons share edges along the *b*-axis forming chains and one FeO_6 octahedron shares edges with one PO_4 tetrahedron and two LiO_6 octahedrons, respectively. At the same time, one PO_4 tetrahedron also shares edges with two LiO_6 octahedrons producing a 1D channel for free intercalation and deintercalation of Li^+ to ensure excellent structural stability during electrochemical cycling. The strong P—O covalent bond in the phosphate group stabilizes the oxygen atoms in the fully charged state and prevents them from being released by oxidation to produce oxygen. Therefore, $LiFePO_4$ has high thermal stability in the lithiated and delithiated states and batteries with the $LiFePO_4$ cathode do not burn easily or explode under thermal runaway. In addition, the price of $LiFePO_4$ is lower than that of $Li(NiCoMn)O_2$ due to the abundance of raw materials and improved preparation procedures.

Besides $LiFePO_4$, other phosphate-based materials such as $LiMnPO_4$,[121,122] $LiCoPO_4$,[123,124] $LiNiPO_4$,[125–127] and $Li_3V_2(PO_4)_3$[128–130] have received research attention due to the high operating voltages that can provide higher energy densities. However, the toxicity of vanadium, high cost of cobalt, low conductivity of manganese-based materials, and high operating

 © 2022 Wiley-VCH GmbH

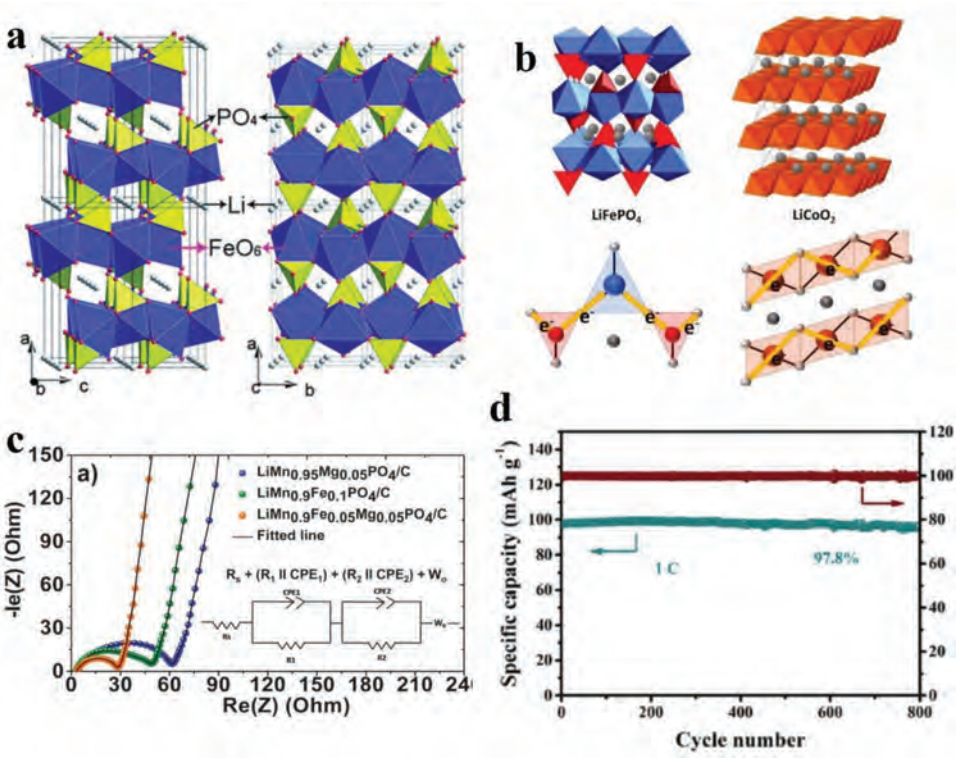

Figure 10. a) Polyhedral representation of the crystal structure of $LiFePO_4$ viewed along the *b*- and *c*-axis, respectively. Reproduced with permission.[120] Copyright 2011, Elsevier. b) Comparison of the electron transport pathways between $LiFePO_4$ and $LiCoO_2$. In $LiFePO_4$, electrons diffuse through O—Fe—O—P—O and the rate is slower than that of O—Co—O in $LiCoO_2$, leading to poor electrical conductivity in polyanion-structured cathode materials. Reproduced with permission.[131] Copyright 2021, American Chemical Society. c) Nyquist impedance spectra of $LiMn_{0.9}Fe_{(0.1-x)}Mg_xPO_4/C$ (x = 0, 0.05, and 0.1). Reproduced with permission.[134] Copyright 2013, Royal Society of Chemistry. d) Long-cycling properties of the NVP@C-3DPS electrode at 1 C for 800 cycles. Reproduced with permission.[140] Copyright 2018, Wiley.

voltage (>4.8 V vs Li/Li^+) of nickel-based materials have hampered the commercialization of these materials.[125] The inherently low electrical conductivity of polyanionic materials also severely limits the electrochemical performance due to the unique atomic arrangement. In $LiMPO_4$, the MO_6 octahedron is separated by the PO_4 tetrahedron, forming the M—O—P—O—M mode of electron transfer which is much slower than that of the M—O—M mode in $LiMO_2$ (Figure 10b).[131] Due to restricted 1D Li diffusion channels in the polyanion crystal structure, ion diffusion is slow and easily blocked. Studies have been carried out to address the issues, for example, coating conductive carbon on the active particles to improve the conductivity, shortening the ion diffusion distance by reducing the particle size of the active materials, and improving the electron/ionic conductivity of the materials by manipulating the crystal structure and electronic environment through metal ion doping.[132–134] Veena et al. have synthesized nanocone-shaped carbon-coated $LiMnPO_4/C$ materials by a modified Pechini method and electrochemical measurements indicate that the $LiMnPO_4/C$ cathode has excellent electrochemical cyclic stability with a capacity of 130.8 mAh g^{-1} after 500 cycles at 0.017 A g^{-1} due to the nanopyramid morphology and carbon coating.[132] Ramar and Balaya have studied the effects of Fe^{2+} and/or Mg^{2+} doping on high-potential olivine $LiMnPO_4/C$ and the electrochemical properties.[134] During Li extraction, the delithiated phase generated by the Fe^{2+}/Fe^{3+} redox (3.45 V) favors the electrochemical activity of the subsequent Mn^{2+}/Mn^{3+} redox. Generation of the lithiated phase from Mg^{2+} provides a favorable environment for subsequent Li intercalation and the electrical conductivity and Li^+ diffusion in the Fe^{2+} and Mg^{2+} codoped samples are improved (Figure 10c). As a result, the $LiMn_{0.9}Fe_{0.05}Mg_{0.05}PO_4/C$ cathode shows excellent electrochemical characteristics such as high discharge capacities of 159 and 51.8 mAh g^{-1} at 0.1 and 10 C, respectively. The strategies of carbon coating and metal ion doping can improve fast charging of $LiMnPO_4$ and can be extended to other phosphate cathodes.

P-based polyanionic compounds are promising cathode materials for NIBs and KIBs. Owing to large-scale application of $LiFePO_4$ to LIBs, $NaFePO_4$ is naturally the preferred cathode materials for NIBs. However, the preparation of olivine-structured $NaFePO_4$ is difficult because $NaFePO_4$ synthesized by conventional chemistry has a maricite phase (m-$NaFePO_4$).[12] The structure of m-$NaFePO_4$ is composed of corner-sharing FeO_6 octahedron and PO_4 tetrahedron and due to the absence of Na^+ transport channel in the structure, m-$NaFePO_4$ is considered nonelectrochemically active in NIBs.[135] Kim et al. have found that m-$NaFePO_4$ is transformed into amorphous $NaFePO_4$ after desorption of Na^+ to reduce the transport barrier of Na^+.[136] The initial discharge-specific capacity of m-$NaFePO_4$ is 142 mAh g^{-1}, which is 92% of the theoretical value and 95% capacity retention is observed after 200 cycles. However, the amorphous structure

 © 2022 Wiley-VCH GmbH

of $NaFePO_4$ has a low working potential (≈2.4 V), making it not suitable for commercial applications.

The NASICON structure is a Na^+ superconductor with a large 3D channel structure, which can achieve rapid insertion/extraction of Na^+. NASICON-type phosphate materials have high working voltage and good structural stability and are promising cathode materials for NIBs.[137] Among the various NASICON-type phosphate materials, $Na_3V_2(PO_4)_3$ (NVP) has the advantages of high Na^+ conductivity, small volume deformation (8.26%), high theoretical specific capacity, and high voltage platform as cathode materials in NIBs. NVP belongs to the hexagonal crystal system and the space group is *R*-3*c*. Its crystal structure is formed by connecting each VO_6 octahedron to three PO_4 tetrahedrons through a shared O atom.[138] Typically, two free Na atoms occupy two oxidation state channels in the lattice. Owing to the strong covalent bonding of $(PO_4)^{3-}$, the framework of NVP does not change during extraction of two Na resulting in a theoretical specific capacity of 117 mAh g^{-1} and excellent electrochemical cyclic stability.[139] Like other phosphate electrode materials, NVP has poor electrical conductivity which can be overcome by combination with highly conductive materials. Wang et al. have prepared NVP@C composites by a simple sol-gel method using citric acid gel-derived carbon as the skeleton and NVP crystals as the constituent unit.[140] The 3D porous framework not only constitutes a conductive network, but also shortens the transportation distance of Na^+. The NVP@C electrode shows an impressive rate of 75.8 mAh g^{-1} at 22.5 A g^{-1} and stable cycle behavior of 91.4% capacity retention after 2000 cycles at 1.2 A g^{-1} (Figure 10d). The method of improving the electronic conductivity of $Na_3V_2(PO_4)_3$ by surface modification can be extended to other NASICON structures to provide the possibility for the development of high-performance cathode materials for NIBs.

3.2. Fluorophosphates

As the inactive mass of polyanionic (XO_4) tetrahedra increases, the gravimetric specific capacity of polyanionic materials deceases significantly, which is not conducive to the improvement of the energy density of AIBs. Increasing the cathode potential is another way to improve the energy density of AIBs. The highly electronegative F^- can further increase the ionic characteristics of the M—O bond and reduce the orbital overlap of the M—O bond to increase the redox potential of the cathode materials.[115,141] Barker et al. have prepared $LiVPO_4F$ as cathode materials for LIBs with a high average voltage of 4.1 V and an initial specific capacity of 120 mAh g^{-1}.[142] This work has led to more research on fluorophosphoric acid cathodes.[142–144] Recently, the fluorophosphate family has been extended to NIBs and KIBs with high operating voltages.[145–148] Similar to $Na_3V_2(PO_4)_3$, $Na_3V_2(PO_4)_2F_3$ also has 3D ion diffusion channels with small volume deformation (2.9%) during electrochemical cycling (**Figure 11**a).[149] Because of the induction effect, the $Na_3V_2(PO_4)_2F_3$ (NVPF) electrode has two higher plateaus of 3.6 and 4.2 V during charging/discharging beneficial to the realization of high-energy-density batteries.[150] Deng et al. have prepared a NVPF/C composite by a simple one-step carbothermal reduction and the NVPF/C (10% carbon content) exhibits excellent electrochemical characteristics with high initial specific capacity of 112.2 mAh g^{-1} at 0.064 A g^{-1}, high capacity retention rate of 72.6% after 500 cycles, and high rate capacity of 64 mAh g^{-1} at high current density of 1 A g^{-1}.[151] Li et al. have prepared a composite with well-dispersed NVPF nanoparticles anchored on rGO by adding isopropanol to water to reduce the surface tension.[152] The well-dispersed NVPF particles anchored on the highly conductive rGO matrix provide fast

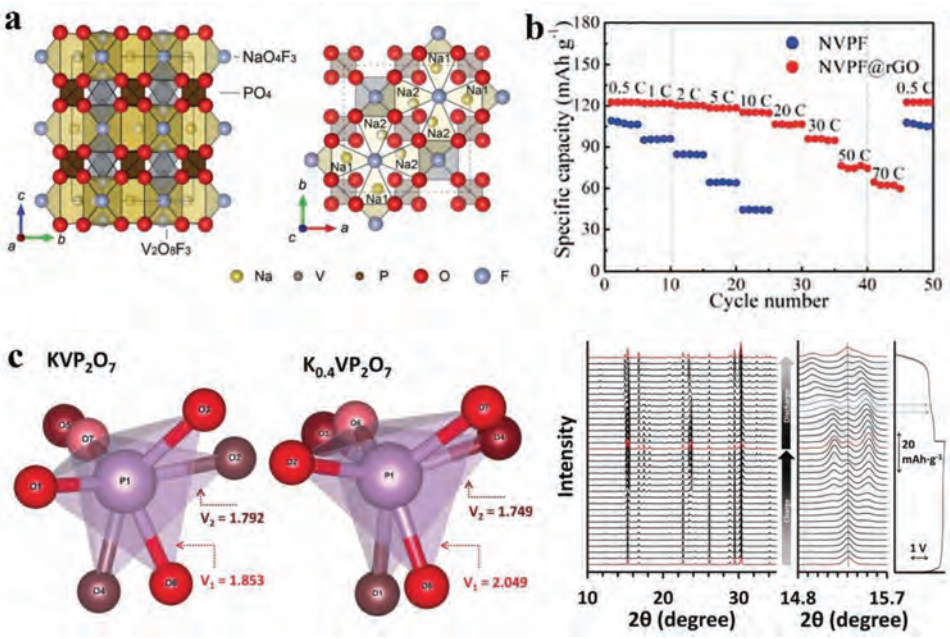

Figure 11. a) Schematic representation of the refined $Na_3V_2(PO_4)_2F_3$ structure and projection. Reproduced with permission.[149] Copyright 2012, Royal Society of Chemistry. b) Rate characteristics of NVPF@rGO between 0.5 C and 70 C. Reproduced with permission.[152] Copyright 2020, Royal Society of Chemistry. c) Conformation of PO_4 tetrahedra in the pyrophosphate units of KVP_2O_7 and $K_{1-x}VP_2O_7$ ($x \approx 0.6$) and in situ XRD spectra of KVP_2O_7 during one charging–discharging cycle (0.25 C, 20 °C). Reproduced with permission.[156] Copyright 2018, Wiley.

 © 2022 Wiley-VCH GmbH

reaction kinetics and good structural stability. The NVPF@rGO electrode has a high reversible capacity of 119 mAh g^{-1} at 0.064 A g^{-1} with almost no capacity decay after 100 cycles and a high reversible capacity of 95 mAh g^{-1} at a high current density of 9.0 A g^{-1} (Figure 11b). However, analysis of the electrochemical mechanism and structure and performance optimization of new high-voltage fluorophosphate cathode materials are relatively few and so research in this area is urgently needed.

3.3. Pyrophosphates

In the temperature range of 500–550 °C, the oxygen atoms in phosphate form pyrophosphate (P_2O_7) and alkali metal pyrophosphate compounds with good thermal stability can be prepared by traditional one-step solid-state synthesis.[153] Alkali pyrophosphate compounds usually consist of transition metal octahedra (MO_6) and P_2O_7 units linked to form a robust framework with multiple alkali ion sites. Due to the size effect of metal ions and great adaptability of P_2O_7 groups, pyrophosphates can form a variety of crystalline structures. However, alkali ions always fit into the available open sites. Compared to phosphates, pyrophosphates have good chemical stability, possible multidimensional ion conduction pathways, and rich crystal structures, which are expected to be the next-generation electrodes for AIBs. Wurm et al. have proposed monometallic pyrophosphate ($LiMP_2O_7$, M = e.g., Fe, V, and Ti) cathodes in 2002.[154] However, the capacity and energy density of these monometallic pyrophosphates are relatively low due to the large molecular weight and low redox potential. The delithium-based metal pyrophosphate ($Li_2MP_2O_7$) is able to provide higher activity of Li^+ and capacity. In particular, $Li_2FeP_2O_7$ is promising as cathode material with a reversible capacity of about 110 mAh g^{-1} and redox potential of 3.5 V.[155] The excellent structural stability of pyrophosphate enables adaptation to intercalation and deintercalation of larger ions (e.g., Na^+, and K^+) and good electrochemical cyclic stability as cathodes in NIBs and KIBs. Sohn et al. have found KVP_2O_7 to be a promising high-energy-density cathodes in KIBs after extensive screening.[156] The galvanostatic charging-discharging results show that KVP_2O_7 has a reversible capacity of 60 mAh g^{-1} and average discharging potential of ≈4.2 V versus K/K^+, corresponding to an energy density of 253 Wh kg^{-1} at 0.25 C. Extraction of K produces a conformational change from the monoclinic KVP_2O_7 to triclinic $K_{1-x}VP_2O_7$ ($x \approx 0.6$), but it can be electrochemically or thermally restored to the intrinsic monoclinic to ensure the structural stability (Figure 11c). Du et al. have synthesized $Li_2FeP_2O_7$/C nanocomposites with different carbon contents by a simple solid-state reaction using cheap glucose as the carbon source.[157] Electrochemical measurements show that the carbon coating and reduced particle size of the active materials improve the electrochemical performance of the $Li_2FeP_2O_7$/C composite. The $Li_2FeP_2O_7$/C composite with carbon content of 4.88 wt% shows the best electrochemical results including a high initial discharge capacity of 103.1 mAh g^{-1} at 0.1 C (corresponding to 93.7% of the theoretical capacity) and high rate capacity of 45.9 mAh g^{-1} at 10 C. Considering the thermal stability of pyrophosphate compounds, screening of the compounds and optimization of nanoscale and carbon coatings are expected to produce breakthroughs in the commercialization of pyrophosphate cathodes.

In this part, various P-based cathode (phosphates, fluorophosphates, and pyrophosphates) and their crystal structure are discussed. It can be seen that different compositions of the polyanion cathode can endow the material with different properties. For example, introducing highly electronegative F^- to the polyanion cathode can increase the potential of polyanion material, thus improving the energy density of AIBs. Besides, by changing the composition of phosphate, pyrophosphate with higher thermal stability can be obtained, achieving higher safety of AIBs. Therefore, the design of P-based polyanion cathode materials needs to be based on specific application scenarios to achieve a better balance between energy density and safety.

4. P-Based Electrolytes and Additives

Electrolytes are carriers for ions in batteries playing the role of transferring ions between the cathode and anode and it is important for AIBs to obtain high voltage and high specific energy. Electrolytes widely used in AIBs are mainly nonaqueous liquid electrolytes and safer solid electrolytes are used less frequently due to the low ionic conductivity. Nonaqueous liquid electrolytes generally consist of organic solvents, electrolyte salts, and additives in a certain proportion. Notably, P compounds have important applications in electrolyte salts, flame retardant additives, and solid electrolytes.

4.1. Electrolyte Salts

P-based materials used as electrolytes in LIBs include $LiPF_6$ and Li salts, in which part of the fluorine is replaced by other groups. $LiPF_6$ is the most widely used Li salts in commercial LIBs and its anion can be regarded as the complex of F^- and Lewis acid PF_5. Owing to the good negative charge distribution of the Lewis acid ligands with the strong electron-withdrawing ability, the corresponding complex salts usually have lower melting points and lower solubility than the low-dielectric media. Because of the poor association ability of PF_6, the conductivity of the $LiPF_6$ electrolyte is high. The conductivity of $LiPF_6$ electrolyte with the EC+DMC (volume ratio 1:1) solution at 20 °C is up to 10×10^{-3} S cm^{-1} and slightly less than that of $LiAsF_6$ and higher than that of other inorganic Li-salts.[158,159] $LiPF_6$ has strong electrochemical stability and the stable voltage of the cathode reaches 5.1 V, which is much higher than the 4.2 V required by LIBs and does not corrode the aluminum current collector.[160] At present, $LiPF_6$ still dominates the commercial Li-salt market because of the comprehensive performance.

However, $LiPF_6$ has some drawbacks, the most obvious ones are chemical and thermal instability. $LiPF_6$ has a low decomposition temperature (only 30 °C) in the air environment. This is because, in the presence of Lewis acid (H_2O), PF_5 will be generated by dissociating F^- from PF_6^- (i.e., $PF_6^- \leftrightarrow PF_5 + F^-$).[161] The generated PF_5 can catalyze the ring-opening of cyclic carbonates and promote the formation of carbonate group-containing

© 2022 Wiley-VCH GmbH

polymers. In this process, the electrolyte is converted to CO_2 and polyethylene oxide.[162] In addition, it is worth noting that a certain amount of impurities (HF and H_2O) have remained in the preparation of $LiPF_6$. This is because HF and H_2O have certain bond energies with $LiPF_6$, which makes them difficult to remove.[163,164] As mentioned above, the Lewis acid of H_2O and HF can promote the production of PF_5, which will harm the stability of $LiPF_6$-containing electrolytes. Therefore, purified $LiPF_6$ is needed for electrolytes with better stability. And when purified $LiPF_6$ is dissolved in organic solvents, the decomposition temperature of $LiPF_6$ can reach 80–130 °C, which avoids the decomposition of $LiPF_6$ at room temperature. In addition, PF_5 can react with trace amounts of water or protonic acids to produce HF, which seriously affects the electrochemical performance of batteries. Various attempts have been made to replace the unstable P—F bonds with more stable ones such as perfluoroalkyl, aryl, or oxyacetyl chelate substituents to improve the chemical stability and thermal stability of $LiPF_6$ while maintaining the inherent advantages.[161] Inspired by the high thermal stability of LiBOB, the unstable fluorine in $LiPF_6$ is fully or partially chelated by oxalate and the chelated grass groups endow graphite anodes with the unique interfacial chemistry and high thermal stability during electrochemical cycling.[165] Xu et al. have studied the cyclic behavior of $LiPF_4(C_2O_4)$ (LiTFOB) with different types of graphite.[166] In the carbonate-based solvent, LiTFOB can perform reversible Li^+ intercalation/extraction on the $LiNi_{0.8}Co_{0.2}O_2$ cathode and graphite anode (**Figure 12**a), and shows superior performance to $LiFP_6$ indicating the formation of a stable interfacial phase.

4.2. Solid Electrolytes

Although liquid electrolytes have the advantages of high ionic conductivity and good contact with electrodes, they have disadvantages such as flammability of solvents, easy leakage, poor safety, complex battery manufacturing, and self-heavy. In recent years, all-solid-state LIBs have become a research hotspot due to their high safety, high energy density, and simple battery structure.

LiPON films are the most widely used solid electrolyte films in all-solid-state thin-film Li batteries because of the low activation energy (0.45 eV), and electrochemical stability window up to 5.5 V.[167] Besides, the interfaces of LiPON with the low electrode potential Li metal anode and the high electrode potential transition metal oxide cathode are very stable. Hood et al. have observed the dynamic evolution of the LiPON–Li interface by in situ electron microscopy. A thin interfacial layer (≈60 nm) is formed at the LiPON–Li interface and it is composed of conductive binary compounds with a unique spatial distribution, which ensures the electrochemical stability of the interface and can be used as an effective passivation layer (Figure 12b).[167] As LiPON is currently the only solid electrolyte that is not affected by dendrite growth and has good electrochemical cycling performance, LiPON can be used as the base materials for the design of high-performance solid Li batteries in the future.[167,168] Cheng et al. have studied the interface between Li metal and LiPON by cryo-electron microscopy.[169] The Li/LiPON interface with a thickness of 76 nm is observed to be composed of SEI components including Li_2O, Li_3N, and Li_3PO_4 with a multilayer mosaic structure of N and P concentration gradients (Figure 12c). The structural and chemical information contributes to a more complete understanding of the cause of interfacial stability and formation mechanism paving the way for high specific energy LIBs.

Li_6PS_5X (X = Cl, Br, I) are promising new sulfide-based Li^+ superconductors with a high room-temperature ionic conductivity of more than 10^{-3} S cm^{-1}. The high ionic conductivity of Li_6PS_5X electrolytes is derived from the tightly packed structure of anionic tetrahedra (cubic unit cell with space group $F43m$), where P fills the tetrahedral gaps to form an isolated PS_4 tetrahedral network, and Li is randomly distributed in the remaining tetrahedral gaps form ion channels.[170] However, all-solid-state batteries based on Li_6PS_5X solid electrolytes have serious interfacial problems (e.g., interfacial reactions, heterointerface incompatibility, and Li dendrite growth). Liu et al. have prepared Li_6PS_5Cl solid electrolyte with a smooth surface by adjusting the sintering time.[171] During the process of densification and sintering, the pores between the Li_6PS_5Cl particles are eliminated, the contact between the particles is improved, and the uniform distribution of charge on the electrolyte surface is promoted, thus inhibiting the growth of Li dendrites. The prepared densified Li_6PS_5Cl solid electrolyte has a high ionic conductivity of 6.11 mS cm^{-1} and a critical current density of 1.05 mA cm^{-2} at room temperature. Solid-state batteries prepared with the densified Li_6PS_5Cl solid electrolyte can cycle steadily for 3000 h. Nan et al. have prepared a composite solid electrolyte membrane (CSE) consisting of arginite-type electrolyte Li_6PS_5Cl and polar polyvinylidene fluoride-copolytrifluoroethylene (P(VDF-TrFE)) skeleton by electrospinning-infiltration-hot pressing.[172] The interaction between Li_6PS_5Cl and polar P(VDF-TrFE) ensures high Li^+ conductivity (≈1.2 mS cm^{-1}) and good mechanical ductility of the composite electrolyte membrane at room temperature. The assembled NCM@LNO‖CSE‖Li-In coin-type all-solid-state battery exhibits excellent electrochemical performance with a capacity retention of 71% after 20 000 cycles at 1.0 mA cm^{-2} (1.61 C). In addition, pouch cells using the CSE exhibit high capacity, further showing their potential for future commercial applications. Zhang et al. have revealed the evolution of the space charge layer of NCM811/ Li_6PS_5Cl /Li batteries by in situ electrochemical impedance spectroscopy and Raman spectroscopy.[173] In the early stage of the cycle, the space charge layer is the main factor affecting the deterioration of the battery interface. The migration and redistribution of Li^+ at the interface caused by the space charge layer (Li^+ transfers from the sulfide side to the oxide side) leads to the interfacial change of P—S bond state in the sulfide electrolyte Li_6PS_5Cl.[173] The increase in battery cycles, interfacial reactions, mechanical failures, and dendrite growth lead to the deterioration of the interface, resulting in the degradation of battery performance. This in-depth interfacial research work provides an important theoretical reference for optimizing all-solid-state batteries.

$Li_{10}GeP_2S_{12}$ (LGPS) solid electrolyte has attracted extensive research interest in recent years due to its extremely high ionic conductivity of about 10 mS cm^{-1}. The unusually high ionic conductivity of LGPS is attributed to its unique crystal structure, in which the S arrays in LGPS more closely resemble the lattice of bcc arrays than the hcp arrays often observed in other

© 2022 Wiley-VCH GmbH

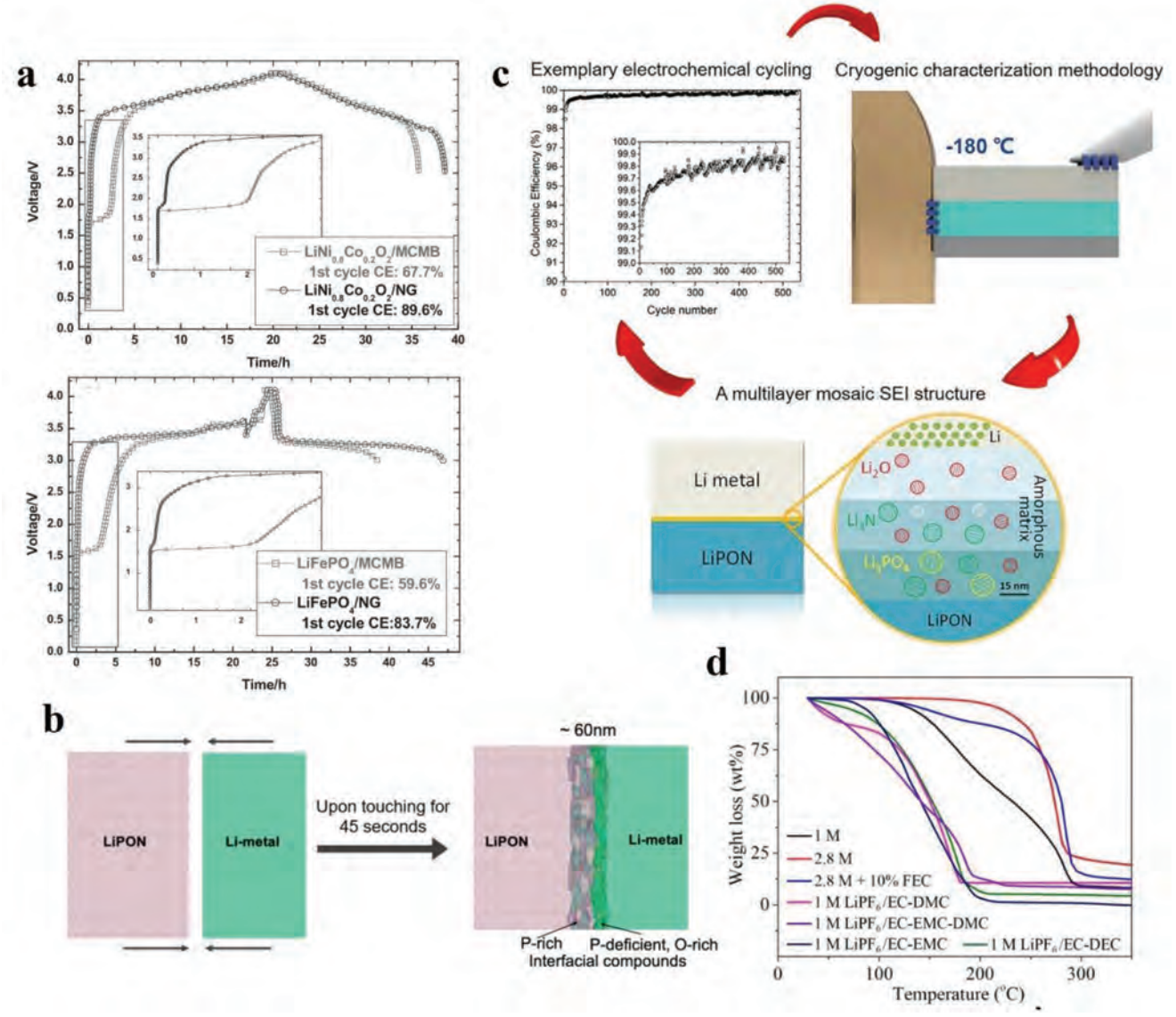

Figure 12. a) Voltage profiles of the MCMB/$LiNi_{0.8}Co_{0.2}O_2$, NG/$LiNi_{0.8}Co_{0.2}O_2$, MCMB/$LiFePO_4$, and NG/$LiFePO_4$ cells with 1.0 M $LiPF_4C_2O_4$ EC/EMC. Reproduced with permission.[166] Copyright 2011, IOP Publishing. b) Schematic representation of interphase formation between the Li metal and LiPON. Reproduced with permission.[167] Copyright 2021, American Chemical Society. c) Schematic representation of the SEI structure of the Li metal and LiPON interface revealed by cryo-electron microscopy. Reproduced with permission.[169] Copyright 2020, Elsevier. d) TG analysis of the TEP-based electrolytes (e.g., 1 M, 2.8 M, and 2.8 M + 10% FEC) and the conventional carbonate electrolytes (e.g., 1 M $LiPF_6$ in EC-DMC, EC-EMC-DMC, EC-EMC, and EC-DEC). Reproduced with permission.[180] Copyright 2019, American Chemical Society.

thiophosphates.[174,175] The sublattice of bcc provides a continuous shared planar tetrahedral path for Li with a low activation energy of 0.15 eV.[174] However, air/moisture instability is a challenge for the commercialization of LGPS. Sun et al. have prepared partially O-substituted $Li_{10}MP_2S_{12}$ (M = Ge or Si) materials, and the formed $Li_{10}GeP_2S_{12-x}O_x$ ($0 \leq x < 0.9$) maintains the *P*42/*nmc* space group structure.[176] The slight contraction of the lattice constant and the stronger electrostatic interaction between O and Li ions lead to a slight decrease in the ionic conductivity of $Li1_0GeP_2S_{12-x}O_x$ ($0.3 \leq x \leq 0.6$) from 10.3 to 8.43 mS cm^{-1} at 298 K. However, the partial substitution of S by O improves the electrochemical stability of LGPS, and this method is expected to explore LGPS materials with high ionic conductivity and high electrochemical stability. On the other hand, the application prospects of LGPS are also limited by the high price of Ge. Bron et al. have prepared $Li_{10}SnP_2S_{12}$ with the same structure as LGPS by replacing Ge with more economical Sn, preserving the *P*42/*nmc* space group.[177] Although the higher grain boundary resistance slightly reduces the overall conductivity of $Li_{10}SnP_2S_{12}$ to 4 mS cm^{-1}, it is only slightly lower than that of $Li_{10}GeP_2S_{12}$. The high ionic conductivity of this new material, coupled with the greatly reduced cost due to the substitution of Sn for Ge, makes $Li_{10}SnP_2S_{12}$ an attractive and affordable electrolyte candidate for solid-state batteries. Besides, Zhao et al. have investigated the chemical-mechanical failure mechanism of single LGPS electrolyte

 © 2022 Wiley-VCH GmbH

particles using an in situ focused ion beam electron microscope.[178] The results show that a single LGPS particle has a strong size effect during the chemical-mechanical destruction process. Reducing the particle size of LGPS to less than 1 µm can effectively avoid the pulverization of LGPS electrolyte. The size effect is due to the balance between the release of elastic energy from the reaction of Li metal with LGPS and the surface energy and other forms of energy from particle fragmentation. The discovery of this size effect provides size-screening guidance for the design of all-solid-state batteries.

4.3. Fire-Retarding Additives

Electrolyte additives are introduced to electrolytes to improve the properties. The amount of electrolyte additives is generally small but it plays a prominent role in improving the overall electrochemical performance of LIBs. Owing to the flammable properties of liquid electrolytes, safety is an important concern for LIBs in hybrid and electric vehicles. P-based organic solvents are often used as flame retardants in electrolytes to delay fire hazards from LIB misuse. With regard to the common organic solvents of alkyl carbonates, hydrogen radicals (H·) can be produced after heating. The resulting H· further reacts with oxy-oxygen radicals (O·) and triggers the production of more radicals. Organophosphorus is decomposed at a high temperature to generate PO· and PO_2· radicals to capture H· and O·, block the propagation of radical reactions, and inhibit combustion of the electrolyte solvents.[161,179]

Organophosphorus flame retardant additives have been widely studied due to the variety, low toxicity, suitable physical properties, good compatibility, and low cost. Common organophosphorus flame retardants for electrolytes are trimethyl phosphate (TMP), triethyl phosphate (TEP), dimethyl methyl phosphonate (DMMP), diethyl ethyl phosphonate (DEEP), and triphenyl phosphate (TPP). The use of organophosphorus flame retardant additives improves the safety of the electrolyte, but affects the electrochemical performance of the battery mainly because the electrochemical window is not wide enough and reductive decomposition often occurs on the anode surface resulting in increased impedance and decreased capacity.[179] In order to improve the flame retardancy of phosphine and reduce the amount of phosphine, it is necessary to modify it further. Moreover, a small amount of film-forming aids such as fluoroethylene carbonate (FEC) can be used in combination to improve the compatibility of P-based fire-retardant with electrodes and avoid unnecessary reductive decomposition. Dong et al. have developed a flame-retardant LiTFSI/TEP electrolyte containing FEC functional additives (2.8 M + 10% FEC) with high thermal stability (Figure 12d).[180] DFT calculation combined with XPS and SEM analysis indicates that FEC with lower LUMO energy than TEP is preferentially reduced to form LiF-rich SEI on the Li metal anode. This inhibits the growth of Li dendrites and prevents the continuous reaction between Li and TEP solvent. Therefore, the Li||$LiFePO_4$ battery using electrolyte with 10% FEC exhibits ultralong cycle life of ≈90% capacity retention after 2000 cycles at 0.17 A g^{-1} and high rate capability of 103 mAh g^{-1} at 0.85 A g^{-1}). The battery with fire-retardant additives has high safety and good electrochemical properties indicating that the non-flammable electrolytes have broad application prospects in LIBs.

Obviously, the composition of electrolyte is one of the dominant factors affecting the performance of batteries, such as the cyclic behavior and safety. The use of P compounds as electrolyte salts, solid electrolytes, and flame retardants for AIBs is a promising way to develop high energy density and high safety batteries. To achieve high-performance AIBs, the composition of electrolytes with P compounds needs to be optimized. The main optimization principle of liquid electrolytes for AIBs is to obtain stable SEI by using high thermal stability, high chemical stability, high ionic conductivity, and wide electrochemical window P compounds (e.g., Li-salt, and additive). In addition, the design principle of solid electrolyte for AIBs is to obtain a stable interface between the electrode and solid electrolyte by studying the structure and chemistry of P compounds and then adjusting the composition of the solid electrolyte.

5. Conclusion and Prospective

In this paper, we systematically review the application and development of P-based materials for AIBs, including P-based anodes, P-based cathodes, and P-based electrolytes. From the perspective of structural design (1D, 2D, and 3D), the research progress of P-based anode materials (red P, black P, and metal phosphides) for AIBs is discussed. By combining P-based anode materials with conductive matrices and controlling the size and morphology, the challenges of electron/ion transport and volume expansion can be overcome and the electrochemical properties such as cyclic stability and rates of P-based anodes can be improved. The advantages and disadvantages of phosphate polyanionic cathode materials including orthophosphate-based, fluorophosphate-based, and pyrophosphate-based compounds for AIBs are discussed and the research progress is described. The crystal structure, Li^+/Na^+ storage mechanism and modification strategy of phosphate cathode materials, intrinsic relationship between the materials composition, structure, and electrochemical properties of the materials are discussed to provide guidance for future modification of phosphate cathode materials as well as exploration and development of new high specific energy phosphate cathode materials. Finally, the application and development of P-based materials for battery electrolytes are discussed, including the effects of P-based electrolyte salts, P-based solid electrolytes, and P-based flame retardants on the electrochemical properties and safety of batteries.

P-based materials are abundant in nature and have excellent overall properties. In recent years, the research and application of P-based materials in the field of power sources have experienced great progress. However, research on P-based anode materials is still in the early laboratory stage and details about the electrochemical mechanism remain unclear. Considering the practical needs for anode materials in the future, the key goals include high energy density, safety, and cycling lifetime. Overall, capacity fading caused by volume expansion of P-based anodes remains a challenge and so further research on the electrode structure design is needed to improve the overall stability including the structural stability and electrochemical stability of electrodes. In addition, in most reported P-based anodes,

© 2022 Wiley-VCH GmbH

the P concentration is quite small and a large portion of the electrode consists of inactive conductive materials or support materials and hence, the overall energy density of the electrode is not dominated by the P materials. At present, most of the synthetic methods of nanostructured P-based anodes are complicated requiring harsh conditions or toxic raw materials rendering large-scale production difficult. It is necessary to develop simpler synthetic processes that use nontoxic raw materials and milder conditions. Recently, Sun et al. have revealed the lithiation/delithiation mechanism of black P via synchrotron radiation, which is different from the previous understanding.[87] Therefore, the electrochemical reaction mechanism of P-based anodes in other AIBs still needs to be further studied.

Compared to other cathode materials, polyanionic phosphates have better safety and cyclic stability boding well for application to electric vehicles. However, defects introduce poor electrical conductivity and low capacity and limit wider applications. It is thus imperative to develop new high specific energy phosphate cathode materials and suitable high voltage electrolytes. In order to provide more accurate scientific guidance for the optimization of the composition and structure of the electrode materials, the electrochemical mechanism of phosphate materials should be studied in depth. A single electrolyte solvent is commonly not suitable for high-performance AIBs, binary and ternary solvents can balance the different chemical properties of each group. Besides, Li-salt and additives can also affect the electrochemical performance of AIBs. Therefore, using binary and ternary solvents, and further developing suitable P-based Li salts, P-based additives, can be expected to further improve the performance of the AIBs. Development and preparation of high-performance P-based batteries based on P-based cathode materials, P-based anode materials, and P-based electrolyte materials have great prospects in the future and adaptive electrolytes for P-based batteries and coordination of P-based anodes and P-based cathodes also need to be systematically studied.

Acknowledgements

L.Z. and L.H. contributed equally to this work. This work was financially supported by the Science and Technology Innovation Commission of Shenzhen (JCYJ20180507182047316), Shenzhen Excellent Science and Technology Innovation Talent Training Project – Outstanding Youth Project (RCJC20200714114435061), Shenzhen – Hong Kong Innovative Collaborative Research and Development Program (SGLH20181109110802117 and CityU 9240014), and Shenzhen – Hong Kong Technology Cooperation Funding Scheme (TCFS) (GHP/149/20SZ and CityU 9440296).

Conflict of Interest

The authors declare no conflict of interest.

Keywords

alkaline metal-ion batteries, $LiPF_6$, low theoretical capacity, metal phosphides, phosphate cathodes

Received: March 22, 2022
Revised: July 20, 2022
Published online: August 26, 2022

[1] J. Ding, W. Hu, E. Paek, D. Mitlin, *Chem. Rev.* **2018**, *118*, 6457.
[2] J. Y. Hwang, S. T. Myung, Y. K. Sun, *Chem. Soc. Rev.* **2017**, *46*, 3529.
[3] C. Choi, D. S. Ashby, D. M. Butts, R. H. DeBlock, Q. Wei, J. Lau, B. Dunn, *Nat. Rev. Mater.* **2019**, *5*, 5.
[4] N. Yabuuchi, K. Kubota, M. Dahbi, S. Komaba, *Chem. Rev.* **2014**, *114*, 11636.
[5] J. C. Pramudita, D. Sehrawat, D. Goonetilleke, N. Sharma, *Adv. Energy Mater.* **2017**, *7*, 1602911.
[6] M. Á. Muñoz-Márquez, D. Saurel, J. L. Gómez-Cámer, M. Casas-Cabanas, E. Castillo-Martínez, T. Rojo, *Adv. Energy Mater.* **2017**, *7*, 1700463.
[7] B. Cao, Q. Zhang, H. Liu, B. Xu, S. L. Zhang, T. F. Zhou, J. F. Mao, W. K. Pang, Z. P. Guo, A. Li, J. S. Zhou, X. H. Chen, H. H. Song, *Adv. Energy Mater.* **2018**, *8*, 1801149.
[8] Y. Wang, P. Niu, J. Li, S. Wang, L. Li, *Energy Storage Mater.* **2021**, *34*, 436.
[9] W. Liu, H. Zhi, X. Yu, *Energy Storage Mater.* **2019**, *16*, 290.
[10] J. Zhu, G. Xiao, X. Zuo, *Nano-Micro Lett.* **2020**, *12*, 120.
[11] Z. Gong, Y. Yang, *Energy Environ. Sci.* **2011**, *4*, 3223.
[12] T. Jin, H. Li, K. Zhu, P. F. Wang, P. Liu, L. Jiao, *Chem. Soc. Rev.* **2020**, *49*, 2342.
[13] E. G. Herbert, W. E. Tenhaeff, N. J. Dudney, G. M. Pharr, *Thin Solid Films* **2011**, *520*, 413.
[14] S. Sicolo, K. Albe, *J. Power Sources* **2016**, *331*, 382.
[15] Q. Xia, W. Li, Z. Miao, S. Chou, H. Liu, *Nano Res.* **2017**, *10*, 4055.
[16] J. Zhou, Q. Shi, S. Ullah, X. Yang, A. Bachmatiuk, R. Yang, M. H. Rummeli, *Adv. Funct. Mater.* **2020**, *30*, 2004648.
[17] W. Li, Z. Yang, M. Li, Y. Jiang, X. Wei, X. Zhong, L. Gu, Y. Yu, *Nano Lett.* **2016**, *16*, 1546.
[18] Y. Liu, Q. Liu, A. Zhang, J. Cai, X. Cao, Z. Li, P. D. Asimow, C. Zhou, *ACS Nano* **2018**, *12*, 8323.
[19] G. A. Li, C. Y. Wang, W. C. Chang, H. Y. Tuan, *ACS Nano* **2016**, *10*, 8632.
[20] L. Wang, X. He, J. Li, W. Sun, J. Gao, J. Guo, C. Jiang, *Angew. Chem., Int. Ed.* **2012**, *51*, 9034.
[21] S. Carenco, I. Resa, X. L.e Goff, P. L.e Floch, N. Mezailles, *Chem. Commun.* **2008**, https://doi.org/10.1039/b802454e2568.
[22] X. Ling, H. Wang, S. Huang, F. Xia, M. S. Dresselhaus, *Proc. Natl. Acad. Sci. USA* **2015**, *112*, 4523.
[23] V. V. Kulish, O. I. Malyi, C. Persson, P. Wu, *Phys. Chem. Chem. Phys.* **2015**, *17*, 13921.
[24] W. Li, Y. Yang, G. Zhang, Y.-W. Zhang, *Nano Lett.* **2015**, *15*, 1691.
[25] Z. Pei, Y. Liu, D. Sun, Z. Zhu, G. Wang, *Chem. Res. Chin. Univ.* **2020**, *36*, 631.
[26] A. Khandelwal, K. Mani, M. H. Karigerasi, I. Lahiri, *Mater. Sci. Eng. B* **2017**, *221*, 17.
[27] Q. Li, D. Yang, H. Chen, X. Lv, Y. Jiang, Y. Feng, X. Rui, Y. Yu, *SusMat* **2021**, *1*, 359.
[28] H. Liu, S. Zhang, Q. Zhu, B. Cao, P. Zhang, N. Sun, B. Xu, F. Wu, R. Chen, *J. Mater. Chem. A* **2019**, *7*, 11205.
[29] N. Yabuuchi, Y. Matsuura, T. Ishikawa, S. Kuze, J.-Y. Son, Y.-T. Cui, H. Oji, S. Komaba, *ChemElectroChem* **2014**, *1*, 580.
[30] G. Chang, Y. Zhao, L. Dong, D. P. Wilkinson, L. Zhang, Q. Shao, W. Yan, X. Sun, J. Zhang, *J. Mater. Chem. A* **2020**, *8*, 4996.
[31] C. Marino, A. Debenedetti, B. Fraisse, F. Favier, L. Monconduit, *Electrochem. Commun.* **2011**, *13*, 346.
[32] W. Li, Z. Yang, Y. Jiang, Z. Yu, L. Gu, Y. Yu, *Carbon* **2014**, *78*, 455.
[33] X. L. Chen, Y. Y. Ma, *Adv. Mater. Technol.* **2018**, *3*, 1800041.
[34] A. Lekawa-Raus, T. Gizewski, J. Patmore, L. Kurzepa, K. K. Koziol, *Scr. Mater.* **2017**, *131*, 112.
[35] G. H. Chen, D. N. Futaba, S. Sakurai, M. Yumura, K. Hata, *Carbon* **2014**, *67*, 318.
[36] M. M. Shokrieh, R. Rafiee, *Mech. Compos. Mater.* **2010**, *46*, 155.
[37] W. J. Li, S. L. Chou, J. Z. Wang, H. K. Liu, S. X. Dou, *Nano Lett.* **2013**, *13*, 5480.

© 2022 Wiley-VCH GmbH

[38] D. Yuan, J. Cheng, G. Qu, X. Li, W. Ni, B. Wang, H. Liu, *J. Power Sources* **2016**, *301*, 131.
[39] X. Jiao, Y. Liu, B. Li, W. Zhang, C. He, C. Zhang, Z. Yu, T. Gao, J. Song, *Carbon* **2019**, *148*, 518.
[40] Y. Zhu, Y. Wen, X. Fan, T. Gao, F. Han, C. Luo, S.-C. Liou, C. Wang, *ACS Nano* **2015**, *9*, 3254.
[41] J. H. Yun, S. Moon, D. K. Kim, J. H. Kim, *Nanomaterials* **2021**, *11*, 3053.
[42] X. Sun, W. Li, X. Zhong, Y. Yu, *Energy Storage Mater.* **2017**, *9*, 112.
[43] Y. Liu, Q. Liu, C. Jian, D. Cui, M. Chen, Z. Li, T. Li, T. Nilges, K. He, Z. Jia, C. Zhou, *Nat. Commun.* **2020**, *11*, 2520.
[44] R. F. Egerton, *Ultramicroscopy* **2013**, *127*, 100.
[45] R. F. Egerton, P. Li, M. Malac, *Micron* **2004**, *35*, 399.
[46] S. Kim, J. Cui, V. P. Dravid, K. He, *Adv. Mater.* **2019**, *31*, 1904623.
[47] J. Song, Z. Yu, M. L. Gordin, S. Hu, R. Yi, D. Tang, T. Walter, M. Regula, D. Choi, X. Li, A. Manivannan, D. Wang, *Nano Lett.* **2014**, *14*, 6329.
[48] S. Liu, H. Xu, X. Bian, J. Feng, J. Liu, Y. Yang, C. Yuan, Y. An, R. Fan, L. Ci, *ACS Nano* **2018**, *12*, 7380.
[49] T. Wang, S. Wei, R. Villegas Salvatierra, X. Han, Z. Wang, J. M. Tour, *ACS Appl. Mater. Interfaces* **2018**, *10*, 38936.
[50] S. Zhang, H. Ying, R. Guo, W. Yang, W. Q. Han, *J. Phys. Chem. Lett.* **2019**, *10*, 6446.
[51] X. Han, Z. Zhang, M. Han, Y. Cui, J. Sun, *Energy Storage Mater.* **2020**, *26*, 147.
[52] J. Qian, D. Qiao, X. Ai, Y. Cao, H. Yang, *Chem. Commun.* **2012**, *48*, 8931.
[53] J. Qian, X. Wu, Y. Cao, X. Ai, H. Yang, *Angew. Chem., Int. Ed.* **2013**, *52*, 4633.
[54] Y. Wang, L. Tian, Z. Yao, F. Li, S. Li, S. Ye, *Electrochim. Acta* **2015**, *163*, 71.
[55] J. Sun, H.-W. Lee, M. Pasta, Y. Sun, W. Liu, Y. Li, H. R. Lee, N. Liu, Y. Cui, *Energy Storage Mater.* **2016**, *4*, 130.
[56] W. Li, S. Hu, X. Luo, Z. Li, X. Sun, M. Li, F. Liu, Y. Yu, *Adv. Mater.* **2017**, *29*, 1605820.
[57] Y. Yan, S. Xia, H. Sun, Y. Pang, J. Yang, S. Zheng, *Chem. Eng. J.* **2020**, *393*, 124788.
[58] B. Tian, B. Tian, B. Smith, M. C. Scott, Q. Lei, R. Hua, Y. Tian, Y. Liu, *Proc. Natl. Acad. Sci. USA* **2018**, *115*, 4345.
[59] M. Buscema, D. J. Groenendijk, G. A. Steele, H. S. J. van der Zant, A. Castellanos-Gomez, *Nat. Commun.* **2014**, *5*, 4651.
[60] L. Bai, L. Sun, Y. Wang, Z. Liu, Q. Gao, H. Xiang, H. Xie, Y. Zhao, *J. Mater. Chem. A* **2017**, *5*, 8280.
[61] L. K. Li, Y. J. Yu, G. J. Ye, Q. Q. Ge, X. D. Ou, H. Wu, D. L. Feng, X. H. Chen, Y. B. Zhang, *Nat. Nanotechnol.* **2014**, *9*, 372.
[62] J. Jiang, Y. Wen, H. Wang, L. Yin, R. Cheng, C. Liu, L. Feng, J. He, *Adv. Electron. Mater.* **2021**, *7*, 2001125.
[63] M. Long, P. Wang, H. Fang, W. Hu, *Adv. Funct. Mater.* **2018**, *29*, 1803807.
[64] M. Wen, J. H. Wang, R. F. Tong, D. N. Liu, H. Huang, Y. Yu, Z. K. Zhou, P. K. Chu, X. F. Yu, *Adv. Sci.* **2019**, *6*, 1970007.
[65] L.-Q. Sun, M.-J. Li, K. Sun, S.-H. Yu, R.-S. Wang, H.-M. Xie, *J. Phys. Chem. C* **2012**, *116*, 14772.
[66] J. D. Shao, C. S. Ruan, H. H. Xie, Z. B. Li, H. Y. Wang, P. K. Chu, X. F. Yu, *Adv. Sci.* **2018**, *5*, 1700848.
[67] C. M. Park, H. J. Sohn, *Adv. Mater.* **2007**, *19*, 2465.
[68] Z. N. Guo, H. Zhang, S. B. Lu, Z. T. Wang, S. Y. Tang, J. D. Shao, Z. B. Sun, H. H. Xie, H. Y. Wang, X. F. Yu, P. K. Chu, *Adv. Funct. Mater.* **2015**, *25*, 6996.
[69] T. Nilges, M. Kersting, T. Pfeifer, *J. Solid State Chem.* **2008**, *181*, 1707.
[70] M. Köpf, N. Eckstein, D. Pfister, C. Grotz, I. Krüger, M. Greiwe, T. Hansen, H. Kohlmann, T. Nilges, *J Cryst. Growth* **2014**, *405*, 6.
[71] L. Li, Y. Zheng, S. Zhang, J. Yang, Z. Shao, Z. Guo, *Energy Environ. Sci.* **2018**, *11*, 2310.
[72] J. Sun, H. W. Lee, M. Pasta, H. Yuan, G. Zheng, Y. Sun, Y. Li, Y. Cui, *Nat. Nanotechnol.* **2015**, *10*, 980.
[73] S. Haghighat-Shishavan, M. Nazarian-Samani, M. Nazarian-Samani, H.-K. Roh, K.-Y. Chung, B.-W. Cho, S. F. Kashani-Bozorg, K.-B. Kim, *J. Mater. Chem. A* **2018**, *6*, 10121.
[74] J. Sun, C. Liu, H. Wang, Y. Cao, X. Han, S. Zhang, H. Wang, Y. Zhang, A. Chen, Z. Yang, J. Sun, *ACS Appl. Energy Mater.* **2021**, *4*, 4112.
[75] Y. Zhang, L. Wang, H. Xu, J. Cao, D. Chen, W. Han, *Adv. Funct. Mater.* **2020**, *30*, 1909372.
[76] H. Liu, Y. Zou, L. Tao, Z. Ma, D. Liu, P. Zhou, H. Liu, S. Wang, *Small* **2017**, *13*, 1700758.
[77] C. Zhang, Y. Ma, X. Zhang, S. Abdolhosseinzadeh, H. Sheng, W. Lan, A. Pakdel, J. Heier, F. Nüesch, *Energy Environ. Mater.* **2020**, *3*, 29.
[78] H. Li, A. Liu, X. Ren, Y. Yang, L. Gao, M. Fan, T. Ma, *Nanoscale* **2019**, *11*, 19862.
[79] R. Meng, J. Huang, Y. Feng, L. Zu, C. Peng, L. Zheng, L. Zheng, Z. Chen, G. Liu, B. Chen, Y. Mi, J. Yang, *Adv. Energy Mater.* **2018**, *8*, 1801514.
[80] X. Sun, Z. Wang, *Appl. Surf. Sci.* **2018**, *427*, 189.
[81] Y. Zhang, N. Dong, H. Tao, C. Yan, J. Huang, T. Liu, A. W. Robertson, J. Texter, J. Wang, Z. Sun, *Chem. Mater.* **2017**, *29*, 6445.
[82] A. Castellanos-Gomez, L. Vicarelli, E. Prada, J. O. Island, K. L. Narasimha-Acharya, S. I. Blanter, D. J. Groenendijk, M. Buscema, G. A. Steele, J. V. Alvarez, H. W. Zandbergen, J. J. Palacios, H. S. J. van der Zant, *2D Mater.* **2014**, *1*, 025001.
[83] Y. Zhang, H. Wang, Z. Luo, H. T. Tan, B. Li, S. Sun, Z. Li, Y. Zong, Z. J. Xu, Y. Yang, K. A. Khor, Q. Yan, *Adv. Energy Mater.* **2016**, *6*, 1600453.
[84] X. Guo, W. Zhang, J. Zhang, D. Zhou, X. Tang, X. Xu, B. Li, H. Liu, G. Wang, *ACS Nano* **2020**, *14*, 3651.
[85] J. Sun, G. Zheng, H. W. Lee, N. Liu, H. Wang, H. Yao, W. Yang, Y. Cui, *Nano Lett.* **2014**, *14*, 4573.
[86] B. Peng, Y. Xu, K. Liu, X. Wang, F. M. Mulder, *ChemElectroChem* **2017**, *4*, 2140.
[87] M. Li, W. Li, Y. Hu, A. A. Yakovenko, Y. Ren, J. Luo, W. M. Holden, M. Shakouri, Q. Xiao, X. Gao, F. Zhao, J. Liang, R. Feng, R. Li, G. T. Seidler, F. Brandys, R. Divigalpitiya, T.-K. Sham, X. Sun, *Adv. Mater.* **2021**, *33*, 2101259.
[88] S. Zhang, Y. Zhang, Z. Zhang, H. Wang, Y. Cao, B. Zhang, X. Liu, C. Mao, X. Han, H. Gong, Z. Yang, J. Sun, *Adv. Energy Mater.* **2022**, *12*, 2103888.
[89] R. Wang, X. Dai, Z. Qian, S. Zhong, S. Chen, S. Fan, H. Zhang, F. Wu, *ACS Appl. Mater. Interfaces* **2020**, *12*, 31628.
[90] Z. Li, Y. Zheng, Q. Liu, Y. Wang, D. Wang, Z. Li, P. Zheng, Z. Liu, *J. Mater. Chem. A* **2020**, *8*, 19113.
[91] X. Li, X. Wang, W. Yang, Z. Zhu, R. Zhao, Q. Li, H. Li, J. Xu, G. Zhao, H. Li, S. Li, *ACS Appl. Mater. Interfaces* **2019**, *11*, 39961.
[92] X. Li, W. Li, J. Yu, H. Zhang, Z. Shi, Z. Guo, *J. Alloys Compd.* **2017**, *724*, 932.
[93] P. Lou, Z. Cui, Z. Jia, J. Sun, Y. Tan, X. Guo, *ACS Nano* **2017**, *11*, 3705.
[94] L. Ran, B. Luo, I. R. Gentle, T. Lin, Q. Sun, M. Li, M. M. Rana, L. Wang, R. Knibbe, *ACS Nano* **2020**, *14*, 8826.
[95] W. Miao, X. Zhao, R. Wang, Y. Liu, L. Li, Z. Zhang, W. Zhang, *J. Colloid Interface Sci.* **2019**, *556*, 432.
[96] W. Li, X. Li, J. Yu, J. Liao, B. Zhao, L. Huang, A. Ali, H. Zhang, J. H. Wang, Z. Guo, M. Liu, *Nano Energy* **2019**, *61*, 594.
[97] F. Han, C. Zhang, J. Yang, G. Ma, K. He, X. Li, *J. Mater. Chem. A* **2016**, *4*, 12781.
[98] H. Zheng, S. Men, X. Huang, Y. Zhou, H. Gao, J. Huang, X. Kang, *J. Mater. Sci.* **2020**, *55*, 9027.
[99] L. Wu, L. Wang, X. Cheng, M. Ma, Y. Wu, X. Wu, H. Yang, Y. Yu, C. He, *Nano Res.* **2021**, *15*, 2147.

 © 2022 Wiley-VCH GmbH

[100] X. Zhao, W. Wang, Z. Hou, G. Wei, Y. Yu, J. Zhang, Z. Quan, *Chem. Eng. J.* **2019**, *370*, 677.
[101] Z. Wang, F. Wang, K. Liu, J. Zhu, T. Chen, Z. Gu, S. Yin, *J. Alloys Compd.* **2021**, *853*, 157136.
[102] Y. Z. Fang, Y. Zhang, K. Zhu, R. Q. Lian, Y. Gao, J. L. Yin, K. Ye, K. Cheng, J. Yan, G. L. Wang, Y. J. Wei, D. X. Cao, *ACS Nano* **2019**, *13*, 14319.
[103] J. Ma, H. Zhang, Y. Xin, S. Liu, Y. Li, L. Yang, G. Xu, T. Lou, H. Niu, S. Yang, *Dalton Trans.* **2021**, *50*, 1703.
[104] J. Liang, G. Zhu, Y. Zhang, H. Liang, W. Huang, *Nano Res.* **2022**, *15*, 2023.
[105] K. Chen, H. n. Guo, W. q. Li, Y. j. Wang, *Chem. Asian J.* **2021**, *16*, 322.
[106] C. Zhu, X. Mu, J. Popovic, K. Weichert, P. A. van Aken, Y. Yu, J. Maier, *Nano Lett.* **2014**, *14*, 5342.
[107] Z. P. Ding, Y. M. Feng, D. T. Zhang, R. Ji, L. B. Chen, D. G. Ivey, W. F. Wei, *ACS Appl. Mater. Interfaces* **2018**, *10*, 6309.
[108] K. S. Huang, B. Li, M. M. Zhao, J. Q. Qiu, H. G. Xue, H. Pang, *Chin. Chem. Lett.* **2017**, *28*, 2195.
[109] S. H. Yang, H. G. Xue, S. P. Guo, *Coord. Chem. Rev.* **2021**, *427*, 213551.
[110] L. Sharma, S. P. Adiga, H. N. Alshareef, P. Barpanda, *Adv. Energy Mater.* **2020**, *10*, 2001449.
[111] S. Lee, S. S. Park, *J. Solid State Chem.* **2013**, *204*, 329.
[112] P. Barpanda, S.-i. Nishimura, A. Yamada, *Adv. Energy Mater.* **2012**, *2*, 841.
[113] M. Tamaru, S. C. Chung, D. Shimizu, S.-i. Nishimura, A. Yamada, *Chem. Mater.* **2013**, *25*, 2538.
[114] A. Kraytsberg, Y. Ein-Eli, *Adv. Energy Mater.* **2012**, *2*, 922.
[115] C. Liu, Z. G. Neale, G. Cao, *Mater. Today* **2016**, *19*, 109.
[116] M. Hirayama, H. Tomita, K. Kubota, H. Ido, R. Kanno, *Mater. Res. Bull.* **2012**, *47*, 79.
[117] Y. Lyu, X. Wu, K. Wang, Z. Feng, T. Cheng, Y. Liu, M. Wang, R. Chen, L. Xu, J. Zhou, Y. Lu, B. Guo, *Adv. Energy Mater.* **2020**, *11*, 2000982.
[118] M. E. Arroyo-de Dompablo, P. Rozier, M. Morcrette, J.-M. Tarascon, *Chem. Mater.* **2007**, *19*, 2411.
[119] X.-G. Yang, T. Liu, C.-Y. Wang, *Nat. Energy* **2021**, *6*, 176.
[120] W.-J. Zhang, *J. Power Sources* **2011**, *196*, 2962.
[121] K. Rajammal, D. Sivakumar, N. Duraisamy, K. Ramesh, S. Ramesh, *Ionics* **2016**, *22*, 1551.
[122] L. J. Chang, S. H. Luo, Z. Y. Wang, Y. G. Liu, Y. C. Zhai, J. J. Zheng, *Rare Metal Mater. Eng.* **2014**, *43*, 1821.
[123] S. Sreedeep, S. Natarajan, V. Aravindan, *Curr. Opin. Electrochem.* **2022**, *31*, 100868.
[124] L. Deng, D. Y. Zhang, Y. Liu, C. K. Chang, *Mater. Res. Innovations* **2014**, *18*, 462.
[125] S. Karthickprabhu, D. Vikraman, A. Kathalingam, K. Prasanna, H. S. Kim, K. Karuppasamy, *Mater. Lett.* **2019**, *237*, 224.
[126] A. Ornek, *Electrochim. Acta* **2017**, *258*, 524.
[127] Y. Zhang, Y. Pan, J. Liu, G. L. Wang, D. X. Cao, *Chem. Res. Chin. Univ.* **2015**, *31*, 117.
[128] H. T. Tan, L. H. Xu, H. B. Geng, X. H. Rui, C. C. Li, S. M. Huang, *Small* **2018**, *14*, 1800567.
[129] Y. S. Hu, X. Ma, P. Guo, F. Jaeger, Z. H. Wang, *J. Alloys Compd.* **2017**, *723*, 873.
[130] G. C. Liu, Y. N. Liu, S. Q. Liu, *Trans. Nonferrous Met. Soc. China* **2013**, *23*, 439.
[131] J. Ling, C. Karuppiah, S. G. Krishnan, M. V. Reddy, I. I. Misnon, M. H. Ab Rahim, C.-C. Yang, R. Jose, *Energy Fuels* **2021**, *35*, 10428.
[132] V. Ragupathi, P. Panigrahi, G. S. Nagarajan, *Appl. Surf. Sci.* **2019**, *495*, 143541.
[133] G. Cai, K. Y. Fung, K. M. Ng, K. L. Chu, K. Hui, L. Xue, *J. Solid State Electrochem.* **2015**, *20*, 379.
[134] V. Ramar, P. Balaya, *Phys. Chem. Chem. Phys.* **2013**, *15*, 17240.
[135] M. Avdeev, Z. Mohamed, C. D. Ling, J. Lu, M. Tamaru, A. Yamada, P. Barpanda, *Inorg. Chem.* **2013**, *52*, 8685.
[136] J. Kim, D.-H. Seo, H. Kim, I. Park, J.-K. Yoo, S.-K. Jung, Y.-U. Park, W. A. Goddard Iii, K. Kang, *Energy Environ. Sci.* **2015**, *8*, 540.
[137] B. Zhang, K. Ma, X. Lv, K. Shi, Y. Wang, Z. Nian, Y. Li, L. Wang, L. Dai, Z. He, *J. Alloys Compd.* **2021**, *867*, 159060.
[138] Z. Jian, W. Han, X. Lu, H. Yang, Y.-S. Hu, J. Zhou, Z. Zhou, J. Li, W. Chen, D. Chen, L. Chen, *Adv. Energy Mater.* **2013**, *3*, 156.
[139] G. Chen, Q. Huang, T. Wu, L. Lu, *Adv. Funct. Mater.* **2020**, *30*, 2001289.
[140] E. Wang, M. Chen, X. Liu, Y. Liu, H. Guo, Z. Wu, W. Xiang, B. Zhong, X. Guo, S. Chou, S. X. Dou, *Small Methods* **2019**, *3*, 1800169.
[141] Z. Yang, G. Li, J. Sun, L. Xie, Y. Jiang, Y. Huang, S. Chen, *Energy Storage Mater.* **2020**, *25*, 724.
[142] J. Barker, M. Y. Saidi, J. L. Swoyer, *J. Electrochem. Soc.* **2003**, *150*, A1394.
[143] H. Y. Asl, A. Choudhury, *RSC Adv.* **2014**, *4*, 37691.
[144] J. Schoiber, R. J. F. Berger, J. Bernardi, M. Schubert, C. Yada, H. Miki, N. Husing, *Cryst. Growth Des.* **2016**, *16*, 4999.
[145] M. Law, P. Balaya, *Energy Storage Mater.* **2018**, *10*, 102.
[146] Q. Liu, D. X. Wang, X. Yang, N. Chen, C. Z. Wang, X. F. Bie, Y. J. Wei, G. Chen, F. Du, *J. Mater. Chem. A* **2015**, *3*, 21478.
[147] R. Ling, S. Cai, D. L. Xie, W. Y. Shen, X. D. Hu, Y. Li, S. S. Hua, Y. Y. Jiang, X. H. Sun, *J. Mater. Sci.* **2018**, *53*, 2735.
[148] H. Kim, D. H. Seo, M. Bianchini, R. J. Clement, H. Kim, J. C. Kim, Y. S. Tian, T. Shi, W. S. Yoon, G. Ceder, *Adv. Energy Mater.* **2018**, *8*, 1801591.
[149] R. A. Shakoor, D.-H. Seo, H. Kim, Y.-U. Park, J. Kim, S.-W. Kim, H. Gwon, S. Lee, K. Kang, *J. Mater. Chem.* **2012**, *22*, 20535.
[150] M. Bianchini, P. Xiao, Y. Wang, G. Ceder, *Adv. Energy Mater.* **2017**, *7*, 1700514.
[151] L. Deng, G. Sun, K. Goh, L.-L. Zheng, F.-D. Yu, X.-L. Sui, L. Zhao, Z.-B. Wang, *Electrochim. Acta* **2019**, *298*, 459.
[152] F. Li, Y. Zhao, L. Xia, Z. Yang, J. Wei, Z. Zhou, *J. Mater. Chem. A* **2020**, *8*, 12391.
[153] P. Barpanda, G. Liu, C. D. Ling, M. Tamaru, M. Avdeev, S.-C. Chung, Y. Yamada, A. Yamada, *Chem. Mater.* **2013**, *25*, 3480.
[154] C. Wurm, M. Morcrette, G. Rousse, L. Dupont, C. Masquelier, *Chem. Mater.* **2002**, *14*, 2701.
[155] S.-i. Nishimura, M. Nakamura, R. Natsui, A. Yamada, *J. Am. Chem. Soc.* **2010**, *132*, 13596.
[156] W. B. Park, S. C. Han, C. Park, S. U. Hong, U. Han, S. P. Singh, Y. H. Jung, D. Ahn, K.-S. Sohn, M. Pyo, *Adv. Energy Mater.* **2018**, *8*, 1703099.
[157] J. Du, L. Jiao, Q. Wu, Y. Liu, Y. Zhao, L. Guo, Y. Wang, H. Yuan, *Electrochim. Acta* **2013**, *103*, 219.
[158] C. W. Walke, Jr., J. D. Cox, M. Salomon, *J. Electrochem. Soc.* **1996**, *143*, L80.
[159] M. Ue, *J. Electrochem. Soc.* **1994**, *141*, 3336.
[160] M. Ue, A. Murakami, S. Nakamura, *J. Electrochem. Soc.* **2002**, *149*, A1572.
[161] K. Xu, *Chem. Rev.* **2014**, *114*, 11503.
[162] S. Wilken, M. Treskow, J. Scheers, P. Johansson, P. Jacobsson, *RSC Adv.* **2013**, *3*, 16359.
[163] A. Zhao, F. Zhong, X. Feng, W. Chen, X. Ai, H. Yang, Y. Cao, *ACS Appl. Mater. Interfaces* **2020**, *12*, 32771.
[164] R. Naejus, D. Lemordant, R. Coudert, P. Willmann, *J. Fluorine Chem.* **1998**, *90*, 81.
[165] U. Wietelmann, W. Bonrath, T. Netscher, H. Noth, J. C. Panitz, M. Wohlfahrt-Mehrens, *Chem. - Eur. J.* **2004**, *10*, 2451.
[166] M. Xu, L. Zhou, D. Chalasani, S. Dalavi, B. L. Lucht, *J. Electrochem. Soc.* **2011**, *158*, A1202.
[167] Z. D. Hood, X. Chen, R. L. Sacci, X. Liu, G. M. Veith, Y. Mo, J. Niu, N. J. Dudney, M. Chi, *Nano Lett.* **2021**, *21*, 151.

© 2022 Wiley-VCH GmbH

[168] J. B. Bates, N. J. Dudney, B. Neudecker, A. Ueda, C. D. Evans, *Solid State Ionics* **2000**, *135*, 33.
[169] D. Cheng, T. A. Wynn, X. Wang, S. Wang, M. Zhang, R. Shimizu, S. Bai, H. Nguyen, C. Fang, M.-c. Kim, W. Li, B. Lu, S. J. Kim, Y. S. Meng, *Joule* **2020**, *4*, 2484.
[170] C. Yu, F. Zhao, J. Luo, L. Zhang, X. Sun, *Nano Energy* **2021**, *83*, 105858.
[171] G. Z. Liu, W. Weng, Z. H. Zhang, L. P. Wu, J. Yang, X. Y. Yao, *Nano Lett.* **2020**, *20*, 6660.
[172] S. J. Liu, L. Zhou, J. Han, K. H. Wen, S. D. Guan, C. J. Xue, Z. Zhang, B. Xu, Y. H. Lin, Y. Shen, L. L. Li, C. W. Nan, *Adv. Energy Mater.* **2022**, *12*, 2200660.
[173] S. Liu, L. Zhou, J. Han, K. Wen, S. Guan, C. Xue, Z. Zhang, B. Xu, Y. Lin, Y. Shen, L. Li, C.-W. Nan, *Adv. Energy Mater.* **2022**, *12*, 2200660.
[174] Y. Kato, S. Hori, R. Kanno, *Adv. Energy Mater.* **2020**, *10*, 2002153.
[175] Y. Wang, W. D. Richards, S. P. Ong, L. J. Miara, J. C. Kim, Y. F. Mo, G. Ceder, *Nat. Mater.* **2015**, *14*, 1026.
[176] Y. L. Sun, K. Suzuki, K. Hara, S. Hori, T. Yano, M. Hara, M. Hirayama, R. Kanno, *J. Power Sources* **2016**, *324*, 798.
[177] P. Bron, S. Johansson, K. Zick, J. Schmedt auf der Günne, S. Dehnen, B. Roling, *J. Am. Chem. Soc.* **2013**, *135*, 15694.
[178] J. Zhao, C. Zhao, J. Zhu, X. Liu, J. Yao, B. Wang, Q. Dai, Z. Wang, J. Chen, P. Jia, Y. Li, S. J. Harris, Y. Yang, Y. Tang, L. Zhang, F. Ding, J. Huang, *Nano Lett.* **2022**, *22*, 411.
[179] S. S. Zhang, *J. Power Sources* **2006**, *162*, 1379.
[180] Y. Dong, N. Zhang, C. Li, Y. Zhang, M. Jia, Y. Wang, Y. Zhao, L. Jiao, F. Cheng, J. Xu, *ACS Appl. Energy Mater.* **2019**, *2*, 2708.

Linchao Zeng is a research assistant in Shenzhen Institutes of Advanced Technology, Chinese Academy of Sciences. He received a Ph.D. degree in 2016 from the University of Science and Technology of China. After obtaining his Ph.D. degree, he began to work as a postdoctoral researcher in Tsinghua University. His research interests mainly include the synthesis and application of nanomaterials for lithium-ion battery, and sodium-ion battery.

Xue-Feng Yu received his Ph.D. degree in Physics from Wuhan University in 2008, and then worked at Wuhan University and City University of Hong Kong. He is currently a professor and director of Materials and Interfaces Center at Shenzhen Institute of Advanced Technology, Chinese Academy of Sciences. He leads an interdisciplinary research group focused on the synthesis and applications of nanomaterials. He has coauthored more than 100 publications in SCI-indexed journals with over 12 000 citations.

© 2022 Wiley-VCH GmbH